CHALMERS

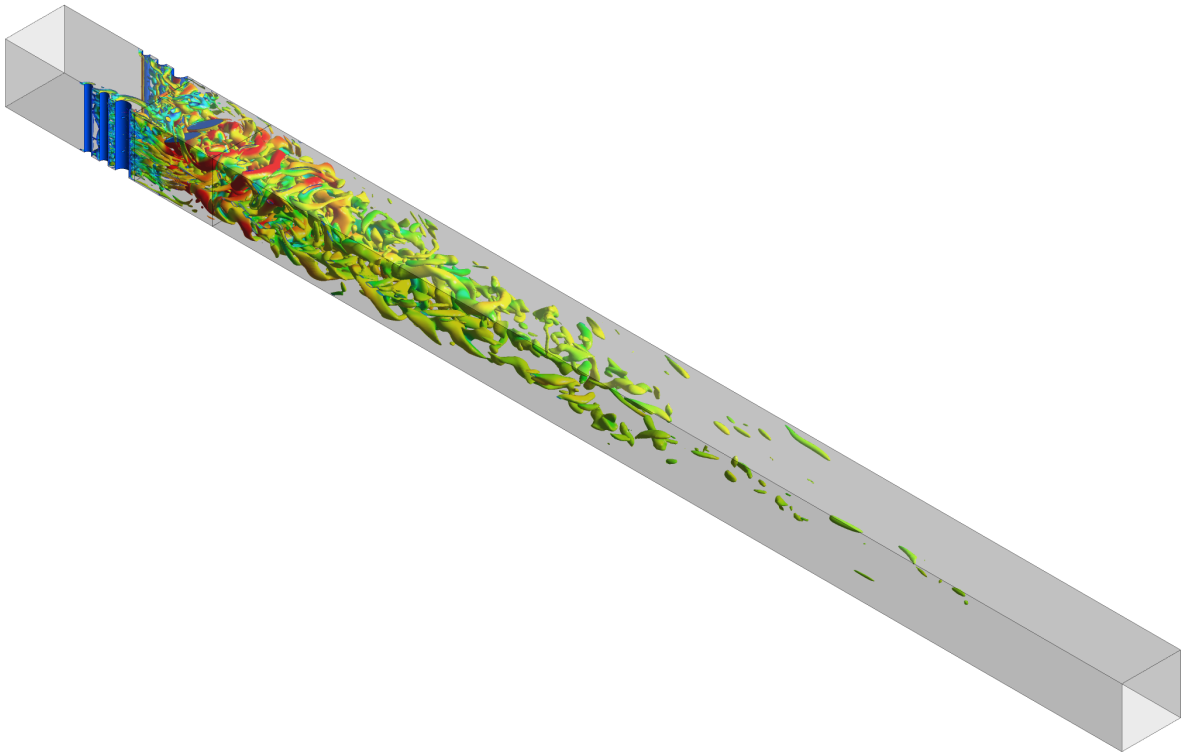

High Fidelity CFD Analysis of a Stationary Mixer

Master's thesis in Applied Mechanics

AXEL BROWN

Department of Applied Mechanics
Division of Fluid Dynamics
CHALMERS UNIVERSITY OF TECHNOLOGY
Göteborg, Sweden 2014
Master's thesis 2014:21

MASTER'S THESIS IN APPLIED MECHANICS

High Fidelity CFD Analysis of a Stationary Mixer

AXEL BROWN

Department of Applied Mechanics
Division of Fluid Dynamics
CHALMERS UNIVERSITY OF TECHNOLOGY
Göteborg, Sweden 2014

High Fidelity CFD Analysis of a Stationary Mixer
AXEL BROWN

Master's thesis 2014:21
ISSN 1652-8557
Department of Applied Mechanics
Division of Fluid Dynamics
Chalmers University of Technology
SE-412 96 Göteborg
Sweden
Telephone: +46 (0)31-772 1000

Cover:
Isosurface of the second invariant of the velocity gradient tensor, Q=5000, representing the instantaneous turbulent structures of the flow in a test rig duct with a stationary mixer

Chalmers Reproservice
Göteborg, Sweden 2014

High Fidelity CFD Analysis of a Stationary Mixer
Master's thesis in Applied Mechanics
AXEL BROWN
Department of Applied Mechanics
Division of Fluid Dynamics
Chalmers University of Technology

Abstract

In the process of cleaning flue gases by chemical reactions, such as with Selective Catalytic Reduction (SCR) cleaning, the performance of the separator device is among others dependent on the mixing of gases before the catalyst region. Hence, in order to develop new products or improve existing ones it is important to have efficient tools to predict the mixing. Previous work using CFD (Computational Fluid Dynamics) on mixing show that there is a need for a more accurate simulation tool than steady state RANS.

This thesis presents a comparative study of the ability of different turbulence models to predict the molecular mixing within an inhomogeneous multi-species fluid mixture in the flow through a SCR duct test rig, for which data is available from laboratory testing. Simulations were carried out using ANSYS-CFX, comparing a steady state RANS model, an unsteady RANS model and a Scale-Adaptive Simulation model (SST-SAS). Three meshes of different densities were used. The models abilities to predict the pressure drop over mixers was also noted.

Results showed that all models proved satisfactory in predicting the pressure drop over the mixers, with the highest accuracy when using SST-SAS on the finest mesh.

It was evident that the RANS models underpredict the mixing whereas the SST-SAS provides results consistent with experimental data. Although the SST-SAS was more computationally demanding than the RANS models, it was concluded that it is more efficient to use turbulence models designed for resolving turbulent motion on a coarse mesh than using time averaging turbulence models on finer meshes.

Keywords: CFD, Mixing, SCR, SST-SAS

Acknowledgements

I wish to express my deepest gratitude to my supervisor, Dr. Robert Moestam at Alstom Power. Thank you for patient and dedicated guidance, encouragement and valuable discussions throughout this entire thesis. Special thanks to my examiner, Professor Lars-Erik Eriksson at the Division of Fluid Dynamics for being available to support and advise me when necessary. I would also like to express my great appreciation to Dr. Abdallah Abou-Taouk at the Division of Fluid Dynamics for generously helping me with ICEM-CFD during the beginning of this project.

Nomenclature

Abbrevations

CFD	Computational Fluid Dynamics
CPU	Central Processing Unit
CV	Coefficient of Variance
DNS	Direct Numerical Simulation
HPC	High Performance Cluster
LES	Large Eddy Simulation
RANS	Reynolds Average Navier-Stokes
RMS	Root Mean Square
SAS	Scale Adaptive Simulation
SCR	Selective Catalytic Reduction
SST	Shear Stress Transport

Upper-case Roman Characters

C_m	Arithmetic average of concentration
CFL	Courant number
D	Kinematic Diffusivity
NO_x	Nitrogen Oxide gases
Q	Second invariant of the velocity gradient tensor
S_{ij}	Strain rate tensor
Sc	Schmidt number
Sc_t	Turbulent Schmidt number
Y_α	Mass fraction of species α

Lower-case Roman Characters

$c(p)$	Concentration in point p
f_i	Body force in the x_i direction
k	Turbulent kinetic energy
p	Static pressure
$\bar{p}$	Time-averaged pressure
p'	Fluctuating pressure
t	Time
u_i	Velocity component i
$\bar{u}_i$	Time-averaged velocity
u_i'	Fluctuating velocity
x_i	Coordinate i

Upper-case Greek Characters

ΔP	Pressure drop
Δt	Time increment
Δx	Nodal spacing

Lower-case Greek Characters

δ_{ij}	Kronecker delta
ε	Turbulent dissipation rate
μ	Dynamic viscosity
μ_t	Turbulent dynamic viscosity
ν	Kinematic viscosity
ν_t	Turbulent kinematic viscosity
ρ	Fluid mixture average density
σ_{ij}	Stress tensor
ω	Specific turbulent dissipation rate

Contents

1 Introduction

ALSTOM Environmental Control System develops, designs, manufactures and markets products for cleaning flue gas from pollutants. In general the harmful component, such as particles, SO_x, NO_x and heavy metals, is separated from the flue gas by chemical reactions, electrically or mechanically, with an efficiency that is limited by gas composition, temperature and local gas velocity. In a gas cleaning product the performance often depends on the uniformity of gas properties such as concentrations and temperature. It is therefore essential to be able to mix gases of various properties before the separation region. There is a large amount of knowledge based on field experience, laboratory test and CFD simulations at ALSTOM, in how to design duct systems to obtain proper mixing.

In order to develop new products or increase the separation efficiency of available products it is vital to have efficient tools to predict the mixing. In general, CFD (Computational Fluid Dynamics) modeling, using steady state RANS two equation turbulence modelling (such as $k-\varepsilon$), suffice to predict trends for industrial applications. However, previous work carried out on mixing shows that there is a need for a simulation tool with higher accuracy in order to predict this phenomenon. Further, as computational cost (time) often is a constraining factor in industrial projects it is of interest to investigate the computational cost required for accurate results.

1.1 Objective

The thesis work aims to show the possibility and cost for accurate mixing simulations, using ANSYS-CFX for specific mixing applications, for which data is available from ALSTOM ECS laboratory in Växjö. This is to be done by performing and analysing comparative simulations using different mesh densities and turbulence models. The simulation models are evaluated based on their ability to predict mixing and pressure loss over mixers and their respective computational cost.

1.2 Scope of work

The intentions of the thesis is not to bring forward recommendations on how to achieve efficient mixing, but rather how the mixing performance can be accurately predicted using CFD. The study is limited to the investigation of three different turbulence models on three meshes of different density.

The idea behind the choice of simulation models was to investigate different groups of simulation models, with the assumption that the results of models within the same group does not vary much in comparison to results of models from different groups. As the industrial standard for most applications when using CFD is steady state RANS models and since this type of models is to act as low mark in terms of predicted mixing, it takes a natural place in this study. The first step towards a transient solver is by employing an unsteady RANS model. This type of model resolves the unsteady mean-flow structures, but is not able to resolve the turbulent fluctuating structures. In order to do so, the next step towards a more sophisticated model is by the use of a RANS/LES hybrid type of model. This will resolve the large scale turbulent structures in unsteady parts of the flow and behave like a RANS model elsewhere. SAS models act similary and can thus also be said to belong to this group of models. The models to be studied in this project are as follows:

- Steady state $k-\omega$ SST model
- Unsteady $k-\omega$ SST model
- SST-SAS $k-\omega$

2 Theory

This chapter will introduce the background and theory which has been the basic foundation in the work of this thesis. Section 2.1 explains some of the physics behind fluid flow and Section 2.2 explains how problems governed by these physics can be solved with the help of computers. In Section 2.3 Selective Catalytic Reduction and some relevant parameters related to mixing are explained.

2.1 Fluid Dynamics

With Fluid Dynamics means the mathematical study of fluids in motion. This chapter will briefly discuss the subject and present theory relevant for this thesis.

2.1.1 Governing equations

This thesis project intends to investigate the molecular mixing in fluid flow with an inhomogeneous multi-species fluid mixture. The physics governing such flow is described in the equations

$$\frac{\partial \rho}{\partial t} + \frac{\partial \rho u_j}{\partial x_j} = 0 \tag{2.1}$$

$$\frac{\partial \rho u_i}{\partial t} + \frac{\partial \rho u_i u_j}{\partial x_j} = \rho f_i + \frac{\partial \sigma_{ij}}{\partial x_j} \tag{2.2}$$

Equation (2.1) describes conservation of mass in a system and is often called the continuity equation. Equation (2.2), often called the momentum equation, states that the rate of change of momentum equals the sum of all forces acting on the control volume. σ_{ij} is called the stress tensor and takes different form depending on material properties and constitutive relations. The constitutive law for Newtonian viscous fluids reads

$$\sigma_{ij} = -p\delta_{ij} + \mu\left(\frac{\partial u_i}{\partial x_j} + \frac{\partial u_j}{\partial x_i}\right) - \frac{2}{3}\mu\frac{\partial u_k}{\partial x_k}\delta_{ij} \tag{2.3}$$

Inserting (2.3) into (2.2) gives

$$\frac{\partial \rho u_i}{\partial t} + \frac{\partial \rho u_i u_j}{\partial x_j} = \rho f_i - \frac{\partial p}{\partial x_i} + \frac{\partial}{\partial x_j}\mu\left(\frac{\partial u_i}{\partial x_j} + \frac{\partial u_j}{\partial x_i} - \frac{2}{3}\frac{\partial u_k}{\partial x_k}\delta_{ij}\right) \tag{2.4}$$

The set of equations in (2.4) is often referred to as the Navier-Stokes equations. They describe the motion of the fluid and can be solved together with appropriate boundary conditions in order to determine the velocity and fluid properties of the flow field. The different species in the mixture share the same flow field, allowing an average density of the mixture to be used, here denoted ρ. However, in order to calculate the species concentration in the fluid one more equation is required, namely a transport equation that describes how a species is transported within the fluid:

$$\frac{\partial}{\partial t}\left(\rho Y_\alpha\right) + \frac{\partial}{\partial x_j}\left(\rho Y_\alpha u_j\right) = \frac{\partial}{\partial x_j}\left[\left(\rho D\right)\frac{\partial Y_\alpha}{\partial x_j}\right] \tag{2.5}$$

where Y_α denotes the mass fraction of species α in the fluid mixture. D denotes the kinematic diffusivity for species α.

After the concentration of species α in a two-component mixture is determined, the concentration of the remaining component in the fluid is calculated by the use of the following expression

$$Y_\alpha + Y_\beta = 1 \tag{2.6}$$

For a multi-component mixture with N species it is thus necessary to use transport equations for $N-1$ species only.

2.1.2 Turbulence

Most flows that are encountered are turbulent, industrial mixing included. Turbulent flows are chaotic, irregular and complex, with fluctuations in flow velocity and pressure. Inertial forces are dominant over viscous forces and unsteady eddies are formed from mechanical energy of the flow. These eddies interact with each other allowing for transport of momentum, energy and other various quantities of the flow. The large-scale eddies are generated by energy from the mean flow. Each eddy gives rise to smaller eddies and energy is thereby being passed on from larger to smaller turbulent scales until the smallest turbulent scales where viscosity becomes dominant and the energy is turned into heat by viscous dissipation. This is referred to as the cascade process.

Turbulence allow for increased transport of various quantities through the fluid. The increased dispersal of momentum gives rise to greater skin friction and drag forces. This together with the heat dissipation in the cascade process makes turbulent flow associated with much larger energy losses than that associated with laminar flow. Further, turbulence also allow for an increased transport of material, making turbulent mixing far superior than mixing in laminar flow.

In the case of industrial mixing, the features of turbulence have an important impact on the performance of the mixer. Turbulence will assure efficient mixing, but also results in a higher pressure drop over the mixer duct, increasing energy costs for the process. Consequently, a good mixer is characterized by the successful tradeoff between good mixing abilities and low pressure losses.

For further reading see: [1]

2.2 Computational Fluid Dynamics

Although there exist simplified cases for which the equations governing the flow can be solved analytically, virtually all industrial flow analyses involves numerical methods to solve the equations. There are many different ways to approach and solve a turbulent fluid flow problem. The most accurate way of doing this is by Direct Numerical Simulation, where the flow is resolved entirely down to the smallest time- and length scales. This approach is extremely computationally demanding and in most cases, one has to resort to other methods in order to compute the flow field. There are many methods available to model the behaviour of the smallest turbulent scales, thus reducing the computational cost substantially. Some of those will be presented below.

2.2.1 RANS Turbulence models

Instead of solving the governing equations of the flow for the instantaneous flow field one can solve the time-averaged Navier-Stokes equations. Assuming incompressible flow ($\rho = constant$), these equations are derived by decomposing the fluctuating variables into one mean part and one fluctuating part according to

$$\begin{aligned} u_i &= \bar{u}_i + u_i' \\ p &= \bar{p} + p' \end{aligned} \tag{2.7}$$

Inserting (2.7) into the governing equations, (2.1) and (2.4) then becomes

$$\frac{\partial \rho}{\partial t} + \frac{\partial \rho \bar{u}_j}{\partial x_j} = 0 \tag{2.8}$$

$$\frac{\partial \rho \bar{u}_i}{\partial t} + \frac{\partial \rho \bar{u}_i \bar{u}_j}{\partial x_j} = \rho f_i - \frac{\partial \bar{p}}{\partial x_i} + \frac{\partial}{\partial x_j}\left[\mu\left(\frac{\partial \bar{u}_i}{\partial x_j} + \frac{\partial \bar{u}_j}{\partial x_i} - \frac{2}{3}\frac{\partial \bar{u}_k}{\partial x_k}\delta_{ij}\right) - \rho\overline{u_i' u_j'}\right] \tag{2.9}$$

These equations are called the Reynolds Averaged Navier-Stokes (RANS) and look much like before apart from the new term on the right, $-\rho\overline{u_i' u_j'}$ called the Reynold Stresses. They add six new unknown variables to the equation system making it impossible to solve directly. The term represents stresses due to turbulent fluctuations and thus it may be close at hand to model these stresses in a way that resembles the viscous stresses on a fluid element. This can be done by the use of Boussinesq assumption, which models the Reynold Stresses as

$$-\rho\overline{u_i' u_j'} = \mu_t\left(\frac{\partial \bar{u}_i}{\partial x_j} + \frac{\partial \bar{u}_j}{\partial x_i} - \frac{2}{3}\frac{\partial \bar{u}_k}{\partial x_k}\delta_{ij}\right) \tag{2.10}$$

This deals with the six unknown Reynolds Stresses, but it introduces yet another unknown variable: the turbulent viscosity μ_t. The turbulent viscosity can be compared to the molecular viscosity of a fluid, although the turbulent viscosity is regarded as a property of the flow rather than a property of the fluid. Thus, via the Boussinesq assumption the turbulent stresses are modelled in analogy to their molecular counterparts.

For the turbulent Reynolds-averaged case, Equation (2.5) now becomes

$$\frac{\partial}{\partial t}\left(\rho Y_\alpha\right) + \frac{\partial}{\partial x_j}\left(\rho Y_\alpha u_j\right) = \frac{\partial}{\partial x_j}\left[\left(\frac{\mu}{Sc} + \frac{\mu_t}{Sc_t}\right)\frac{\partial Y_\alpha}{\partial x_j}\right] \tag{2.11}$$

It can be seen here that the kinematic diffusivity term is split up in one laminar and one turbulent part. Sc denotes the so called Schmidt number, which describes the ratio of viscous diffusion rate to mass diffusion rate. Sc_t is the turbulent Schmidt number, describing the ratio of momentum diffusion to mass diffusion due to turbulence, in accordance with Reynolds analogy.

As mentioned before, with the use of Boussinesq assumption there is still one too many unknown variables in the equation system. The turbulence viscosity μ_t, or the kinematic turbulent viscosity ν_t needs to be modelled. There are several ways in which this can be done, of which the ones used in this project will be presented below.

The $k-\varepsilon$ model

The $k-\varepsilon$ model uses the turbulent kinetic energy, k and the dissipation of turbulent kinetic energy, ε to find an expression for the turbulent viscosity according to

$$\mu_t = \rho C_\mu \frac{k^2}{\varepsilon} \tag{2.12}$$

where C_μ is a dimensionless constant. Together with (2.12) are transport equations for k and ε, the so called k-equation and ε-equation.

The $k-\varepsilon$ model is very commonly used and widely validated turbulence model. It has shown good agreeability to many types of flows in industrial applications without the need to change the model variables. However, the model performance is reportedly poor in for example unconfined flows, rotating flows and flows with adverse pressure gradients, [2].

The $k-\omega$ model

The $k-\omega$ model is much like the $k-\varepsilon$ model but it models the turbulent viscosity in terms of the turbulent kinetic energy, k and the specific dissipation rate of turbulent kinetic energy, $\omega \propto \frac{\varepsilon}{k}$. Along with an equation for the turbulent viscosity are transport equations for k and ω. The equation for the turbulent viscosity reads

$$\mu_t = \rho \frac{k}{\omega} \tag{2.13}$$

The $k-\omega$ model is more accurate than the $k-\varepsilon$ model at predicting near-wall flow and flows with adverse pressure gradients. Its main disadvantage is that results are highly sensitive to the value of ω in the free stream [3, 4].

The $k-\omega$ SST model

This model is a combination of the $k-\omega$ and the $k-\varepsilon$ models. It utilizes the strengths of both models by using the $k-\omega$ in the boundary layer and the $k-\varepsilon$ in the free stream. The result is a model that is well suited for a larger selection of flow fields.

In the $k-\omega$ SST model, the turbulent viscosity is limited according to Equation (2.14) for improved performance in a variety of flows.

$$\mu_t = \frac{\rho a_1 k}{max(a_1\omega; SF_2)} \tag{2.14}$$

where $S = \sqrt{2S_{ij}S_{ij}}$, a_1 is a constant and F_2 is a blending function. The corresponding transport equations are stated as follows:

$$\frac{\partial}{\partial t}(\rho k) + \frac{\partial}{\partial x_j}(\rho k u_j) = \frac{\partial}{\partial x_j}\left[\left(\mu + \frac{\mu_k}{\sigma_k}\right)\frac{\partial k}{\partial x_j}\right] + P_k - \beta^*\rho\omega k \tag{2.15}$$

$$\frac{\partial}{\partial t}(\rho\omega) + \frac{\partial}{\partial x_j}(\rho\omega u_j) = \frac{\partial}{\partial x_j}\left[\left(\mu + \frac{\mu_k}{\sigma_\omega}\right)\frac{\partial \omega}{\partial x_j}\right] + \rho\beta\omega^2 + C_\omega + \alpha S^2 \tag{2.16}$$

where P_k is the rate of production of turbulent kinetic energy, C_ω is the cross-diffusion term and αS^2 is the rate of production of ω, [2, 3, 5]

URANS vs RANS

When performing RANS simulations, one makes a distinction between steady state RANS and unsteady state RANS (or URANS). The latter includes all the terms stated in the RANS equations above, whereas the former removes the time dependent terms from the equations. Consequently, RANS simulations provide a steady state time-averaged solution of the flow whereas URANS is able to resolve mean-flow fluctuation and produces a solution of a time-averaged flow that can vary in time.

Hereinafter, the steady state $k-\omega$ SST model will be referred to as the RANS model and the unsteady $k-\omega$ SST will be referred to as the URANS model.

2.2.2 The SST-SAS $k-\omega$ model

This model presented by Menter and Egorov (2005) is based upon the unsteady $k-\omega$ SST model but has an additional term in the ω equation. This term, called the SAS-term provides information about the von Kármán length-scale, allowing the model to better detect unsteady fluctuations. In effect, this means that the model dynamically adjusts which parts of the turbulence spectrum to be modelled or resolved. In unsteady parts of the flow field, more of the turbulent structures will be resolved, whereas the model will behave like a steady RANS model in the stable regions of the flow.

The equations for the turbulent viscosity, μ_t and the turbulent kinetic energy, k are identical to that of the $k-\omega$ SST model. The transport equation for ω reads

$$\frac{\partial}{\partial t}(\rho\omega) + \frac{\partial}{\partial x_j}(\rho\omega u_j) = \frac{\partial}{\partial x_j}\left[\left(\mu + \frac{\mu_k}{\sigma_\omega}\right)\frac{\partial \omega}{\partial x_j}\right] + \rho\beta\omega^2 + C_\omega + \alpha S^2(1 + P_{SAS}) \tag{2.17}$$

$$P_{SAS} = \xi_2\kappa\frac{L}{L_{vK,3D}}, L_{vK,3D} = \kappa\frac{S}{U''}$$

where S and U'' are generic first and second velocity derivatives and $L_{vK,3D}$ denotes the von Kármán length scale.

The SST-SAS $k-\omega$ model has in many cases shown improved results compared to RANS/URANS simulations although it demands a higher computational effort. For more details and information, see [6]-[14].

Hereinafter, the SST-SAS $k-\omega$ model will be referred to as the SST-SAS model.

2.3 Selective Catalytic Reduction and mixing

Selective Catalytic Reduction (SCR) is a method of converting NO_x-gases into N_2 and H_2O with the help of a gaseous reducing agent, usually ammonia, and a catalyst. SCR systems are typically used with for example petrol or diesel engine exhaust gases or power plant flue gases, where the reducing agent is injected to the exhaust/flue gas stream before entering the catalyst. For an effective chemical reaction in the catalyst it is essential that gases are properly mixed, with a uniform gas concentration profile before the separation region. If the mixing is insufficient, this may result in unacceptably low NO_x conversions or the undesirable release of the reducing agent into the atmosphere.

2.3.1 Important parameters

Generally, it is desirable to achieve good mixing at the shortest distance possible and with the lowest possible pressure drop over the mixer. In order to evaluate the performance of a mixer system, it can be quantified with a number of parameters, some of which will be presented below.

The Coefficient of Variation (CV)

The Coefficient of Variation (or CV) is normalized measure of dispersion on a quantity of a statistical population. If the measured quantity is concentration, CV essentially expresses how well a species in a gas mixture is mixed. The definition for CV reads

$$CV = \frac{\text{Standard Deviation}}{\text{Mean}} = \frac{1}{\sqrt{n-1}} \sqrt{\sum_{p=1}^{n} \left(\frac{c(p) - C_m}{C_m} \right)^2} \tag{2.18}$$

where n is the number of measurement points, $c(p)$ is the concentration of the gas species measured at measurement point p and C_m is the arithmetic average concentration of the gas species over all the measurement points. Measurements are usually made over a cross section of a duct so that CV expresses the mixing at that section.

Specific mixing length (L/S)

Typically, it is of interest to express how well the gas is mixed as a function of distance from the nozzles. For comparative purposes, it is often convenient to normalize the distance. In this thesis, the specific mixing length is defined as L/S, where L is the distance from the nozzles along the duct and S is the distance between nozzles in the injection grid.

Essentially, when comparing mixing performance between systems, it is expressed in terms of CV for a given distance L/S from the nozzles.

Pressure loss

The pressure drop over a mixer is obtained by measuring the pressure drop over a duct flow with mixers inside and making the difference from the measured pressure drop over the same duct but without mixers:

$$\Delta P_{\text{Mixer}} = \Delta P_{\text{Duct with mixer}} - \Delta P_{\text{Duct without mixer}} \tag{2.19}$$

3 Method

Since the work of this project concerns evaluation of different computational methods it is of interest to explain not only the methodology related to the computational model and simulations, but also how the experimental data was obtained. Therefore, although the execution of the experiments was not a part of the thesis project, they will still be treated here, followed by an explanation of the computational model.

3.1 Test rig experiments

The test rig was arranged to be able to replicate part of the flow dynamics of a real plant. The injection of ammonia into the flow of flue gas in a real plant was simulated with the injection of a trace gas into a flowing stream of air through the test rig.

A number of experiments were conducted with different mixer configurations and flow velocities to quantify mixing capabilities of different mixers. Below is described the specific experimental setup that formed the basis for the computational model and the work of this thesis.

3.1.1 Geometry

The test rig essentially consisted of an 8 m long straight duct with a square cross section of width 0.5 m. Two rows of three half-cylinders each and a total of four injectors fitted inside the duct constitutes a piece of the repeating pattern of multiple injectors and cylinders that are aligned in a full-scale industrial Ammonia Injection Grid.

The injectors were located at the third half-cylinders, pointing in the direction of the air flow and with the outlet in line with the half-cylinder centre. Four elliptic mixer plates were located downstream of the injector nozzles, one mixer plate for each injector. These were arranged in a diverging configuration, with a total blocking area equal to 30 % of the duct cross section. Figure 3.1 shows a schematic view of the duct and the positioning of the different parts.

The outlet diameter on the injector nozzles was 6 mm. The four injectors were carefully manufactured and orifices with diameters of 3 mm were used to throttle the flow. This was done to ensure an even flow distribution out of the injectors, which was also confirmed to have been achieved by velocity measurements.

A grid was mounted at the duct inlet with the purpose of creating an even flow pattern upstream of the gas injectors. The flow through the duct was driven by a fan connected downstream of the duct.

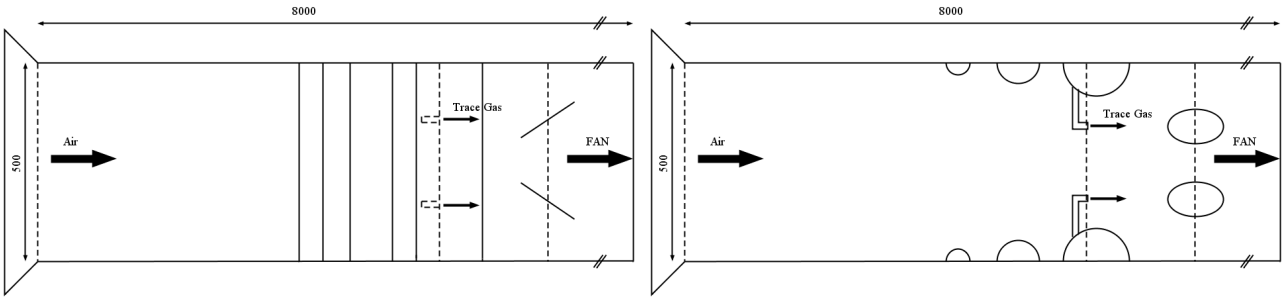

(a) *Side-view* (b) *Top-view*

Figure 3.1: *Schematic view of duct and positioning of parts*

3.1.2 Operating conditions and measurements

During the experiments, the flow velocity was 16 m/s on both the air flowing through the duct as well as the trace gas jet streams from the injectors.

Trace gas concentration measurements were made over six cross sections of the duct, at different distances from the injector nozzles. At each test section a total of 36 measurement were made at locations according to the pattern in Figure 3.3. With information about the trace gas concentration distributed across a test section, the corresponding CV was calculated according to (2.18).

Since the flow where the mixing occurs is turbulent, flow quantities will be fluctuating over time. Trace gas levels were therefore measured as 5 secondes time average. Further, the concentration measurements were made using an analogue IR gas analyser, which itself possess a certain degree of uncertainty.

Tests were also carried out to measure the pressure loss over the entire duct, both with and without mixers present. The pressure loss over the mixers was then calculated according to Equation (2.19).

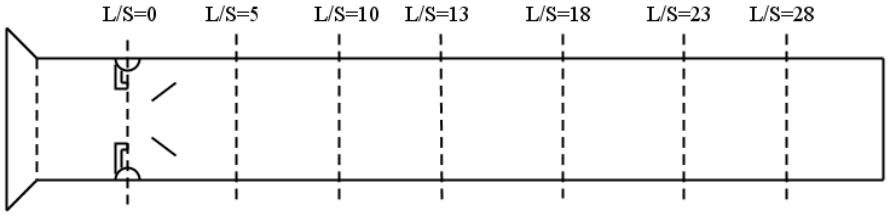

Figure 3.2: *Schematic view of cross sections subjected to trace gas measurements*

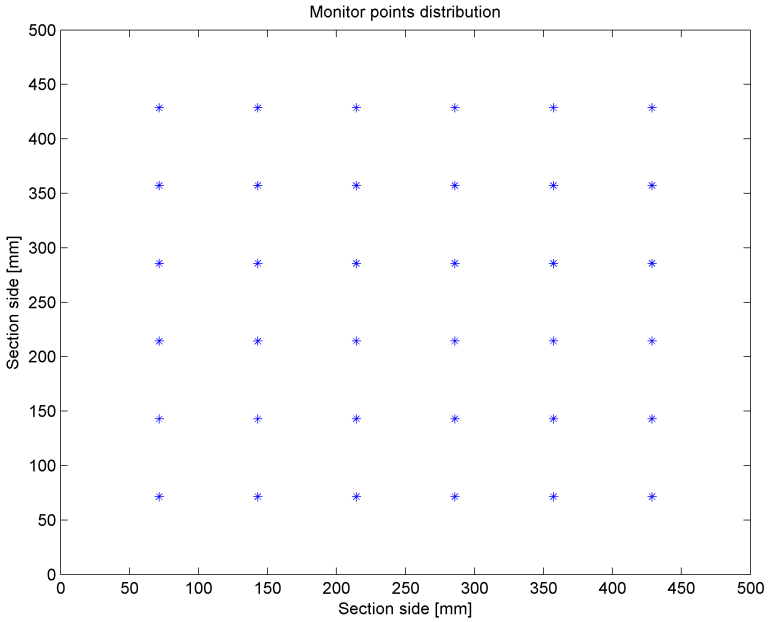

Figure 3.3: *Illustration of monitor point distribution over a duct cross section*

3.2 The computational model

The computational model was setup with the aim to resemble the real experiments in every aspect, trying to rule out sources of errors so that results could be attributed to the turbulence model of choice and/or the

computational mesh. Geometry and mesh generation as well as simulations and post-processing were carried out using software from the ANSYS workbench platform (ICEM CFD for geometry and mesh generation, CFX for simulations and CFD-post for post-processing). The model and simulations are explained in steps below.

3.2.1 Geometry

The geometry of the computational model was similar to that of the physical test rig, with the major difference being an extension to the duct of 500 mm at the outlet in the model. This was done since the furthermost downstream plane to be measured for trace gas concentration would otherwise be located right at the outlet boundary of the model. This would also be considered a source of uncertainty, thus the extension.

Other modifications made to the model includes the removal of the inlet nozzle and a small displacement of parts of the injector tube, none of which are believed to affect the results.

3.2.2 Monitoring of trace gas concentration

To simulate the measurements of the experiments, monitor points were defined in the domain at locations corresponding to those that were being measured in the experiments; six planes with 36 monitor points in each. A view of the model's embodiment and the distribution of monitor points in the domain can be seen in Figure 3.4. These monitor points were set up to record the trace gas concentration for every time step/iteration during simulation, allowing for a time averaged trace gas concentration to be calculated at each monitor point. By analysing time history plots of trace gas concentration for a number of monitor points it could be estimated at what time the flow in the duct had become fully developed, thus ensuring that the time averaging was made over the appropriate time period.

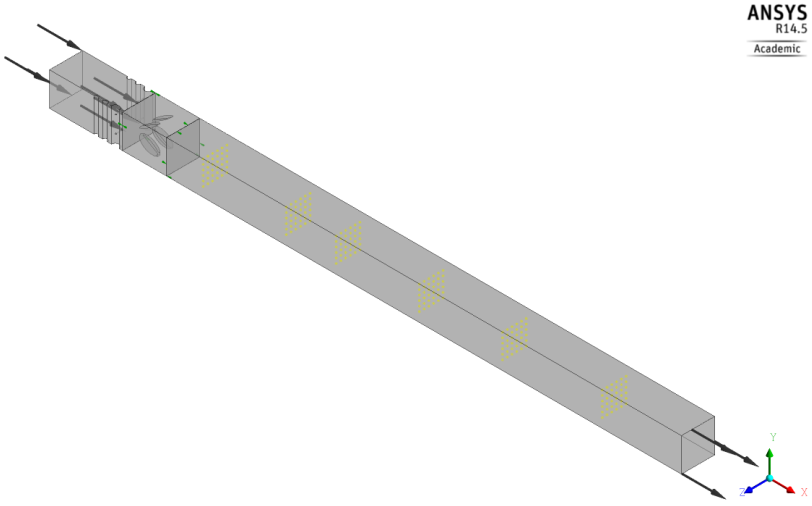

Figure 3.4: *View of computational model, monitor points marked in yellow*

3.2.3 Computational meshes

When performing CFD simulations, the properties of the mesh will influence the results. The mesh can be generated using many different techniques of which each has its strengths and weaknesses. For CFD in industrial applications, time is often a limiting factor, so when choosing meshing strategy both solution quality and overall time efficiency has to be considered. Consequently, unstructured tetrahedral grids are many times used since they allow for a high degree of automated grid generation, which means less effort and time spent on grid generation. However, for large computational analyses, the actual simulation time becomes of greater importance and a little more time spent on mesh generation might still be favourable. Structured hexahedral meshes usually reduce the total element count 4 to 10 fold compared to its tetra-based counterpart for the same spatial resolution [15]. This saves both computational time and resources. Furthermore, hexahedral grids

are generally considered to be more accurate than tetrahedral meshes and allows for a higher degree of user control. For example, when investigating solution sensitivity to different mesh densities, if a mesh structure is already in place the spatial resolution can be changed very easily.

In this thesis project three different computational grids of varying densities were generated. Mainly by reason of computational time and user control, a block-structured approach was used when meshing. The same basic blocking structure was then used for all three meshes.

To obtain a high quality mesh, a number of general guidelines were followed, including to keep aspect ratio and growth ratio of adjacent cells low, avoid cell element skewness and keep good cell orthogonality. The mesh quality was checked using the built in tools in ICEM CFD that evaluates the parameters mentioned above, and improved until desirable quality was achieved. The lower limit mesh quality value was set to 0.4, which is a commonly used limit in ICEM CFD and can be considered to correspond to a good quality mesh.

For each mesh, a version without mixers was also generated. This was done by setting the mixer wall surfaces to interfaces, thus treating the mixers as air while keeping the same nodal structure. Below follows a presentation of the different meshes.

Original Mesh

The generation of the first mesh included building the block structure that also worked as a starting point for making the finer as well as the coarser grid. The mesh contained of approximately 4.77 million cell elements. The mesh domain with the mixers had a distribution of about 240 x 260 cells elements over the duct cross section. In order to keep the number of elements down, the grid near duct walls and half-cylinders was not refined enough for boundary layer flows to be properly resolved. Resolving wall boundary layers was considered inefficient resource utilization, since this part of the flow is not much of interest in regards to mixing. Instead, the flow of primary interest is around and downstream of the mixer plates, where most of the mixing contributing physics occur. This region was also where the finest mesh resolution was found. Cell element sizes were about 4 mm in the flow direction and $0.5 - 1$ mm perpendicular to the flow near the mixer plate walls, allowing for vortex shedding to be better captured. A higher resolution is also found around the injectors, mainly because such a small geometry requires a small nodal spacing in order to be represented with satisfactory accuracy in the model.

Since there are no geometric obstacles to the flow downstream the mixers, a grid interface was placed here to enable one single block to capture the rectangular shape of the duct and to avoid unnecessary propagation of the block structure from upstream. Mass and momentum flux were set to be conserved over the interface. To avoid numerical instability across the interface, cell sizes were kept approximately same in both the streamwise and crosswise direction.

The cell aspect ratio towards the inlet and outlet of the duct was increased and became more elongated in the flow direction. This saved a significant amount of cells and was not believed to impair the results.

Fine Mesh

The fine mesh was essentially based on the same mesh as the original. The focus here was on redistributing the existing elements to achieve a higher quality mesh, coarsening regions with stable flow and refining areas of interest. Mesh refinements were focused to the area around and directly downstream of the mixer plates. The size of the finest cells were again about 4 mm in the flow direction and 0.5-1 mm in the direction perpendicular to the flow near the mixer plate walls. In the finest mesh, the area around the mixers was isolated as a second grid interface was placed between the injectors and mixer plates (see Figure 3.5), making mesh refinement in this region easier and preventing unnecessary extra cells to be added outside the region. Further, the grid interface provides a section cut that separates the peculiar block structure from the injector inlets upstream to affect the nodal distribution downstream and allows for a flow aligned block structure downstream.

The total number of cells was approximately 7.24 million and the mesh domain over the mixers had a cell distribution of about 260 x 340 over the duct cross section.

As with the original mesh, the aspect ratios at the inlet and outlet were kept relatively high (see Figure 3.8).

Coarse Mesh

With the fine mesh as a starting point, the coarse mesh was generated with the aim of making a mesh with a more uniform nodal distribution throughout the domain. This mesh arrangement resembles more the computational grids used in the industry for similar applications, where automated meshing tools are used and cell sizes cannot be controlled on such detailed level. The areas with the finest cell elements were coarsened while the other areas were not significantly changed. Consequently, the typical cell size was approximately 10 mm in all directions, although elements around the injectors were not possible to coarsen since this would cause them to be inaccurately represented. The total cell count was approximately 1.32 million with about 110 x 130 cells occupying the cross section of the domain over the mixers.

(Figures 3.5-3.8) show comparisons between the coarse and fine mesh. Corresponding figures of the original mesh are found in Appendix A.

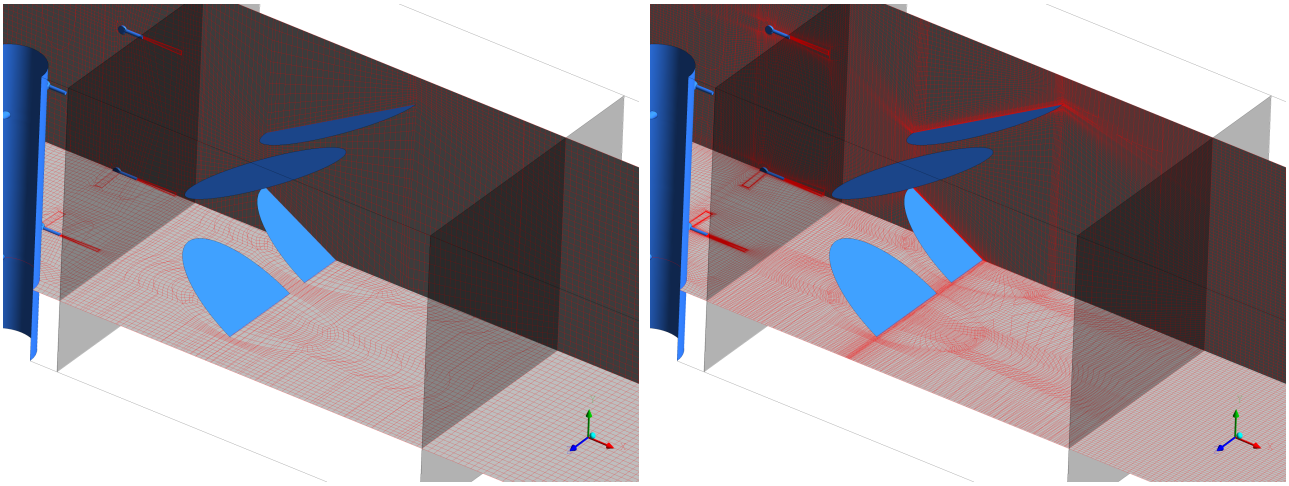

(a) *Coarse Mesh* (b) *Fine Mesh*

Figure 3.5: *Side view of mesh at two planes through the center of a mixer plate. Shadowed sections indicate grid interfaces*

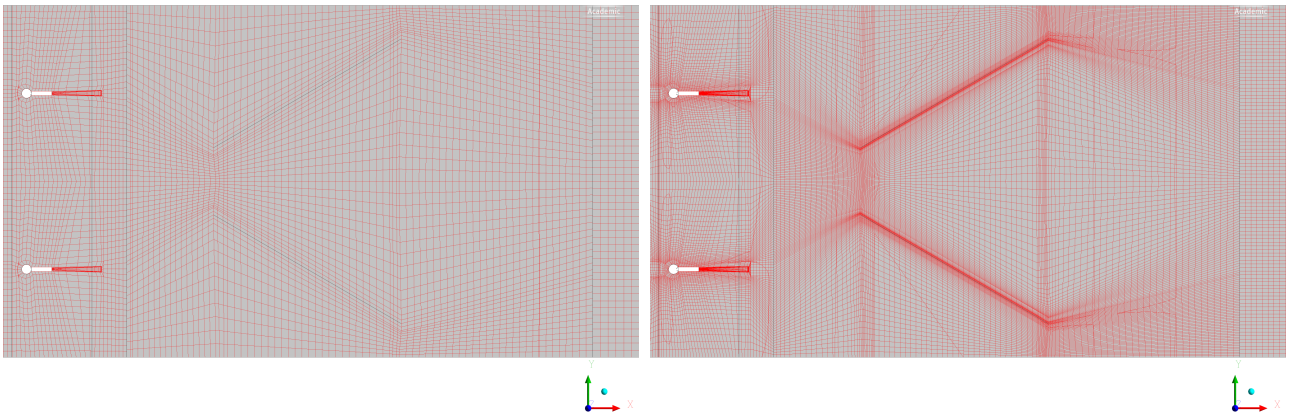

(a) *Coarse Mesh* (b) *Fine Mesh*

Figure 3.6: *View of mesh at X-Y plane through the center of a mixer plate*

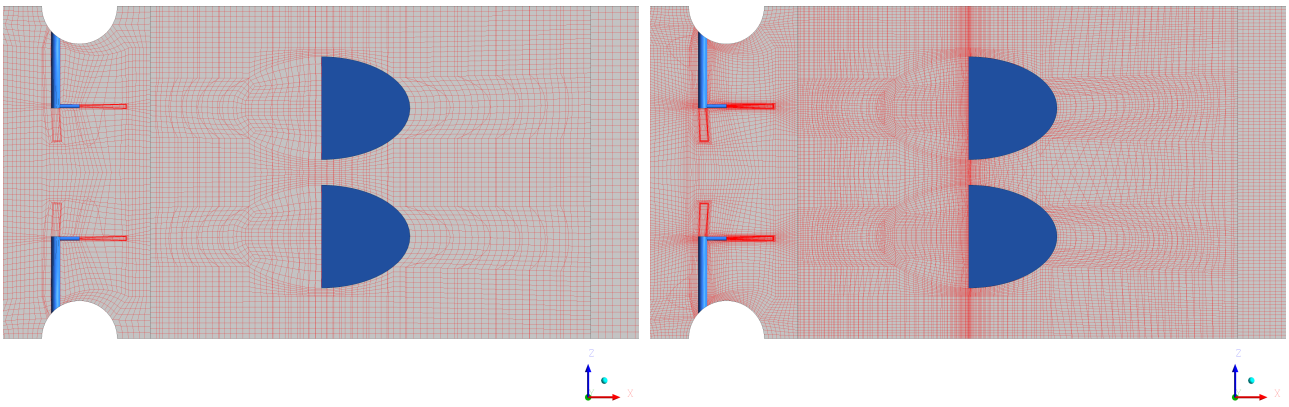

(a) *Coarse Mesh* (b) *Fine Mesh*

Figure 3.7: *View of mesh at X-Z plane through the center of a mixer plate*

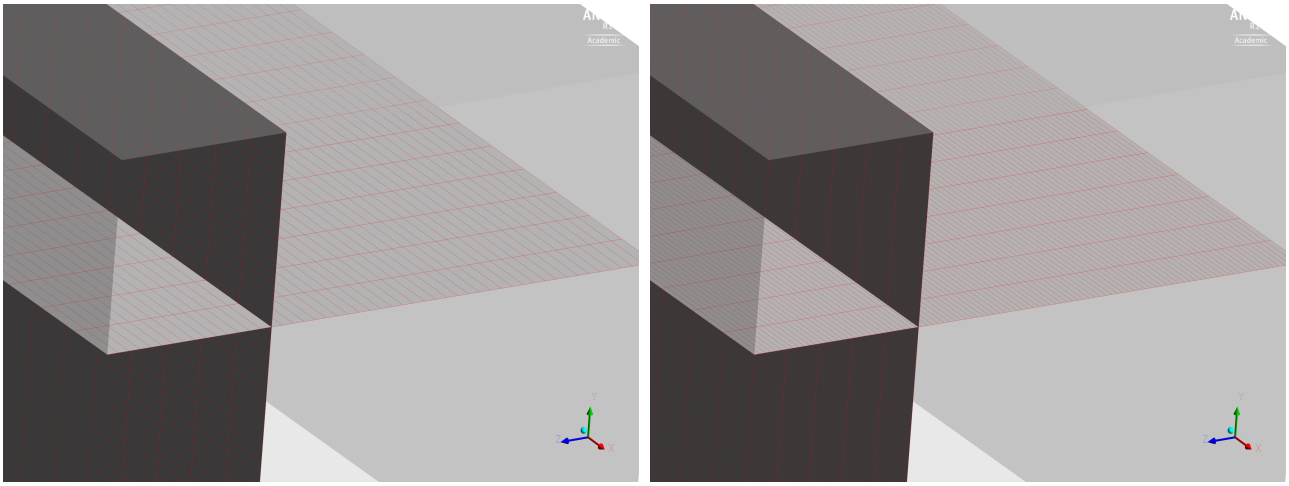

(a) *Coarse Mesh* (b) *Fine Mesh*

Figure 3.8: *Plane sections illustrating mesh aspect ratio at duct outlet*

3.2.4 Boundary conditions

The duct inlet was defined as a velocity inlet with 100 % concentration of air at a velocity of 16 m/s. The duct outlet was defined as a pressure outlet. This model setup is believed to be the most suitable representation of the physics of the flow in the test rig, even though the flow in the test rig was driven by a suction fan downstream of the outlet. The grid throttling at the inlet of the test rig duct generates a stable and even inflow, which is best represented by a velocity inlet boundary condition. The boundary at the injector was set to a velocity inlet with 100 % concentration of the trace gas and a velocity of 16 m/s. The remaining geometry, the mixer plates and duct walls, were defined as no-slip wall, meaning that the flow velocity is zero at the wall.

The fluid material was defined as a variable composition mixture between Air at 25℃ and the trace gas at Standard Pressure, both defined as constant properties gases. Material properties and boundary conditions are stated in Table 3.1.

Table 3.1: Model Boundary conditions and properties

Boundary/property	**Condition**	**Specification**	**Test rig set up**
Inlet	Velocity inlet	100 % Air at 16 m/s	Grid inlet
Trace gas-injection	Velocity inlet	100 % Trace gas at 16 m/s	Velocity inlet
Outlet	Pressure outlet	-	Suction fan
Mixer plates	No-slip wall	-	-
Duct walls	No-slip wall	-	-
Grid interface	Mass and momentum flux conservation	-	-
Reference pressure	-	1 $atm = 101325\ Pa$	-
Air density	-	1.185 kg/m^3	-
Trace gas density	-	1.205 kg/m^3	-

3.2.5 Cases and simulation setups

Several combinations of turbulence models and meshes were tested during the project. The setup was systematically changed in order to investigate the effect on the results. For explanatory reasons, the different simulations can be divided into cases. Each case was based on a specific mesh, on which one simulation respectively of RANS, URANS, SST-SAS and RANS without mixer plates was performed. All the cases followed consistent simulation settings for the different turbulence models in order to simplify evaluation and comparisons between cases and turbulence models. The settings can be seen in Table 3.2.

For each mesh, the RANS simulation was performed first, using a uniform velocity field of air at 16 m/s as initial condition. The results from the RANS simulations were then used as initial conditions for the respective URANS and SST-SAS simulations. Since RANS are generally considered reasonable accurate on predicting pressure distribution in channel flows, it was considered sufficient to simulate the duct without mixer plates using RANS only. This sums up to the total amount of 12 simulations performed to form the basis of the analysis.

A minor investigation on sensitivity to time step size and coefficient loop iterations was conducted. This was done to ensure that convergence was achieved for each time step, so that this would not affect the simulation results. Rather conservative means were taken and no major effort was made on optimization with regards to simulation time. Sensitivity to time step setup was investigated on the finest mesh and then decided upon. Same settings were then used for all three meshes, making the time step setup on the coarser meshes even more conservative. ANSYS CFX is an implicit solver and does therefore not require the Courant number (see definition below) to be small for numerical stability. However, for transient simulations where some of the turbulent scales are resolved, the Courant number needs to be sufficiently small if the transient details are to be resolved accurately [16]. For this reason, the time steps were set to 1 ms for the SST-SAS simulations compared to 2.5 ms for the URANS simulations. Also, one extra URANS simulation with 1 ms time steps instead of 2.5 ms was performed on the original mesh, for comparative reasons.

The Courant number (CFL) is defined as

$$CFL = \frac{u\Delta t}{\Delta x} \tag{3.1}$$

where u is the flow velocity, Δt is the time step size and Δx is the nodal spacing.

The simulation time for all unsteady simulations was set to 3.5 s, which corresponds to more than six flow passages through the duct, thus ensuring the flow to reach a developed state in the simulation.

Table 3.2: Simulation time step and iteration settings

	Turbulence model		
	RANS	**URANS**	**SST-SAS**
Iterations	2000	-	-
Total simulation time	-	3.5 s	3.5 s
Timestep increment	-	2.5 ms	1 ms
Iterations per timestep	-	4	4

4 Results

In this chapter simulation results will be presented and compared with the data acquired from the experiments described in Section 3.1. Section 4.1 consists of an overview of the flow field with figures of velocity distribution and iso-surfaces of Q, the second invariant of the velocity gradient tensor. In Section 4.2, the agreement between simulations and experiments will be presented and discussed. This includes a comparison in CV values, thus the model's ability to predict mixing. In Section 4.3, the correspondence in pressure drop over the duct and loss coefficient between simulation results and experimental data is presented and discussed. Section 4.4 consists of a presentation and discussion of computational cost as well as simulation convergence.

4.1 Flow field overview

Figures 4.1a, 4.1c and 4.1e show the time-averaged (RANS) and instantaneous (URANS and SST-SAS) velocity flow fields on two perpendicular cross sections through a mixer plate on the coarse and fine mesh. As can be seen, small wakes are formed near the wall behind the half-cylinders and injectors. When reaching the mixers the fluid is forced around and accelerated, forming a region of high velocity gradients behind the mixers. Consequently, this is where the highest turbulent activity can be expected.

The RANS and URANS simulations on the coarse mesh are showing very similar results: a symmetric, smooth flow field only with high velocity and velocity gradients immediately downstream the mixers that are quickly decaying into an even flow. In contrast, the SST-SAS solution is showing much higher turbulence activity, visualized by asymmetric velocity fluctuations that starts at the mixers and propagates far downstream.

Looking at similar illustrations with results from simulations on the fine mesh (Figures 4.1b, 4.1d and 4.1f), it can be seen that the calculated flow field does not change much with finer mesh, although some details may be better resolved. The RANS and URANS simulations still predict flow fields that are much alike, even though the URANS simulation now produces an asymmetrical velocity distribution, indicating an unsteady, time-dependent solution.

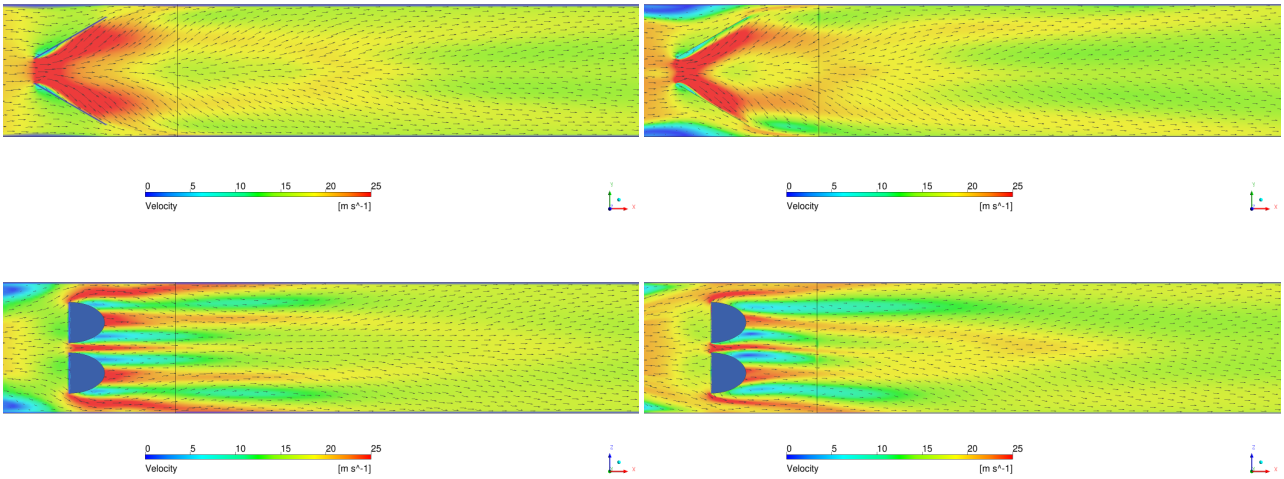

(a) *RANS, coarse mesh*

(b) *RANS, fine mesh*

(c) *URANS, coarse mesh*

(d) *URANS, fine mesh*

(e) *SST-SAS, coarse mesh*

(f) *SST-SAS, fine mesh*

Figure 4.1: *Velocity magnitude at X-Y and X-Z cross sections, coarse and fine mesh*

A common way to visualize turbulent coherent structures and identify vortices is by the use of the second invariant of the velocity gradient tensor (denoted Q). Figures 4.2 and 4.3 show iso surfaces of Q=5000 on the coarse and fine mesh simulations respectively. Figures 4.2a and 4.2a represent the time-averaged steady state RANS solution whereas Figures 4.2b, 4.2c, 4.3b and 4.3c are instantaneous illustrations of Q. Further, an illustration of the time-averaged Q for SST-SAS on the fine mesh can be seen in Figure 4.3d.

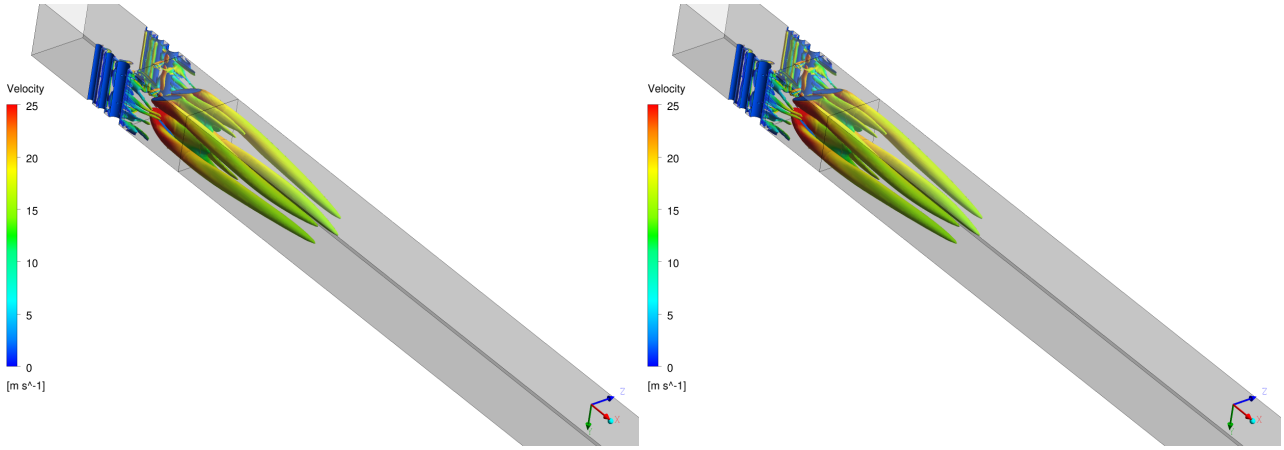

(a) *RANS*

(b) *URANS*

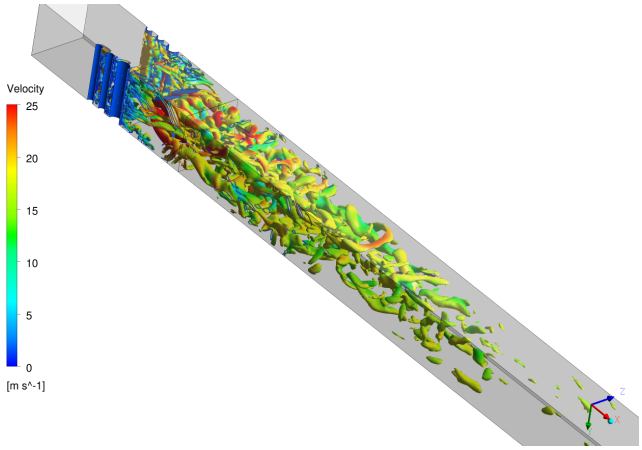

(c) *SST-SAS*

Figure 4.2: *Iso surfaces of Q=5000, coarse mesh (color indicates velocity magnitude)*

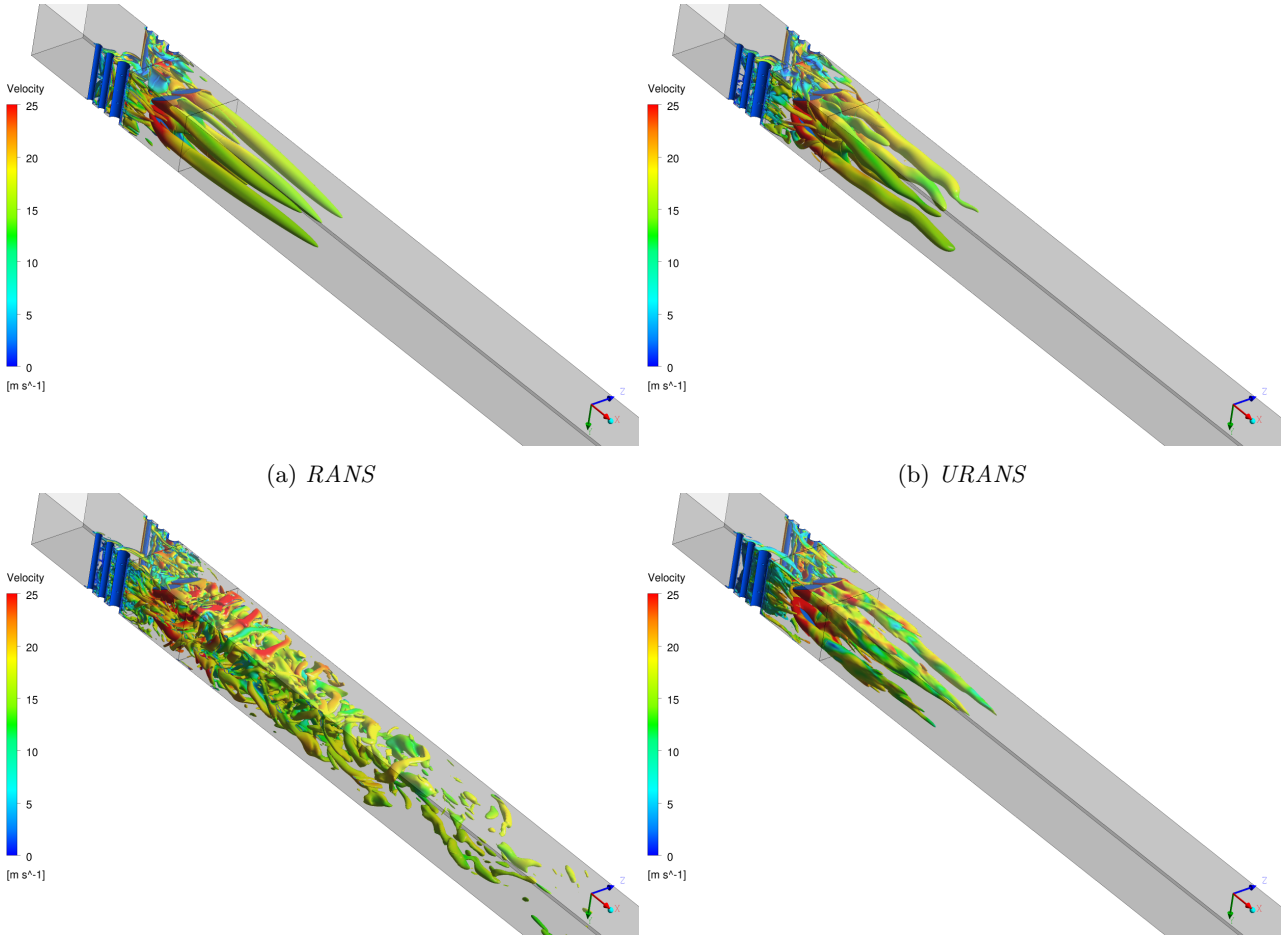

(a) *RANS* (b) *URANS*

(c) *SST-SAS* (d) *SST-SAS, Time averaged*

Figure 4.3: *Iso surfaces of Q=5000, fine mesh (color indicates velocity magnitude)*

Again, the RANS and URANS models are producing noticeable different results from that of the SST-SAS. RANS and URANS models resolve smaller vortices that are formed behind the injectors and half-cylinders and only the large far-stretched coherent structures downstream the mixers. The instantaneous flow field of the SST-SAS simulations however, show significantly more turbulent flow structures behind the mixers that are also stretching further downstream before they dissipate. Even though there is a big difference in flow field, the concentration of the coherent structures of the SST-SAS is greatest at the location of the time-averaged structures found in the RANS and URANS simulations. Further, looking at Figure 4.3d it can be seen that the time averaged SST-SAS is similar to that produced by the RANS and URANS simulations. This indicates that RANS and URANS only captures the time-averaged and most distinct turbulent structures of the flow and fails to capture smaller local turbulent fluctuations.

Figures of the flowfield for simulations on the original mesh can be found in Appendix B.

4.2 Mixing

The calculated CV values at different distances from the nozzles from simulation results are presented in Table 4.1. The measured CV values from experiments are stated as < 3 % due to uncertainties and limited accuracy of equipment and method in the measurements. However, it can be interpreted from the experimental data that most mixing occurs at distances $L/S < 10$ from the nozzles. It also gives an order of magnitude of what CVs could be expected throughout the duct.

Table 4.1: Mixing results from simulations

Mesh	**Simulation model**	**CV125, L/S=5**	**CV250, L/S=10**	**CV325, L/S=13**	**CV450, L/S=18**	**CV575, L/S=23**	**CV725, L/S=28**
	Experiment	-	< 3 %	< 3 %	< 3 %	< 3 %	< 3 %
Coarse	RANS	78.7 %	26.8 %	18.2 %	11.4 %	9.3 %	6.8 %
	URANS	78.7 %	26.8 %	18.2 %	11.4 %	9.3 %	6.8 %
	SST-SAS	39.4 %	4.7 %	2.4 %	1.1 %	0.8 %	0.5 %
Original	RANS	67.3 %	19.5 %	13.6 %	9.6 %	7.0 %	5.1 %
	URANS	68.1 %	16.7 %	10.6 %	5.5 %	3.6 %	2.5 %
	SST-SAS	21.3 %	2.7 %	1.2 %	0.5 %	0.3 %	0.3 %
Fine	RANS	72.0 %	20.9 %	14.6 %	11.4 %	8.4 %	6.0 %
	URANS	66.8 %	15.0 %	9.9 %	5.0 %	3.3 %	2.4 %
	SST-SAS	16.8 %	1.7 %	1.1 %	0.6 %	0.4 %	0.2 %

Looking at the mixing predictions from the coarse mesh simulations, it is noted that RANS and URANS produce strikingly similar results. The predicted mixing is in poor agreement with experimental data throughout the whole duct. Results from the SST-SAS simulation however shows better resemblance to experiments, predicting a CV of the same order of magnitude already at L/S=10. It is also noted that the SST-SAS model detects higher frequency velocity fluctuations compared to the RANS and URANS simulations (see Figure 4.4), which presumably is more comparable to the real flow field.

Figure 4.4 shows the time history of trace gas concentration at a monitor point at L/S=10 for all three turbulence models on the coarse and fine mesh. It is seen that the URANS model on the coarse mesh is not producing a transient solution as intended, but rather oscillates around the steady state RANS solution. This suggests that unsteady RANS simulations on a mesh too coarse will not be able to reproduce the turbulent transient behaviour of the flow, but instead converges to a steady state solution.

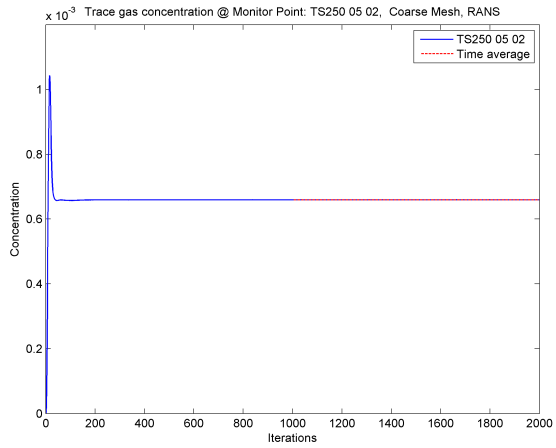

(a) *RANS, coarse mesh*

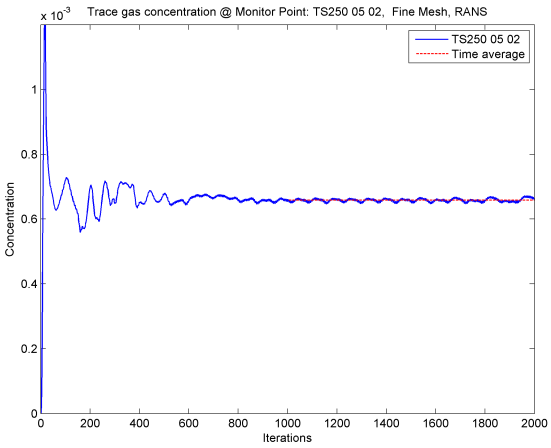

(b) *RANS, fine mesh*

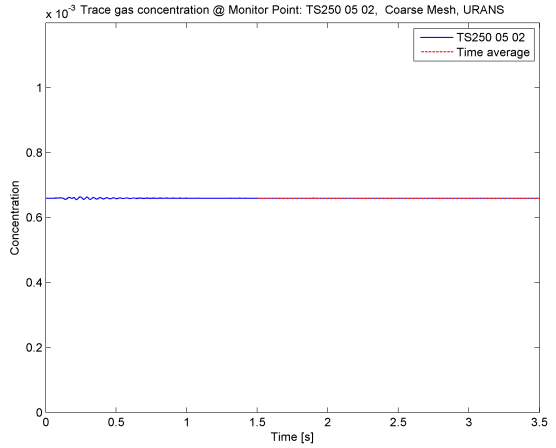

(c) *URANS, coarse mesh*

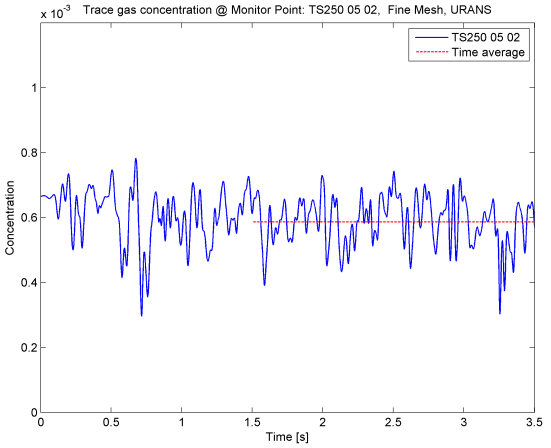

(d) *URANS, fine mesh*

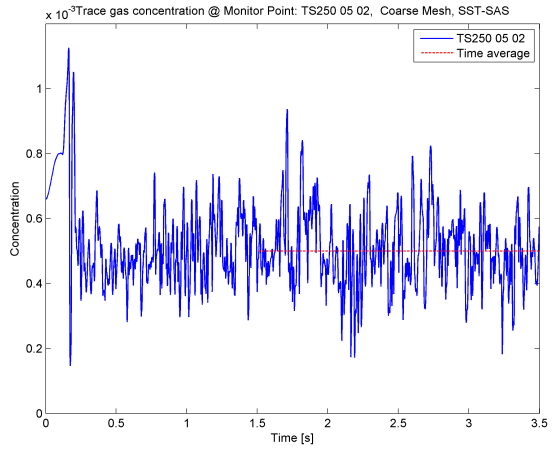

(e) *SST-SAS, coarse mesh*

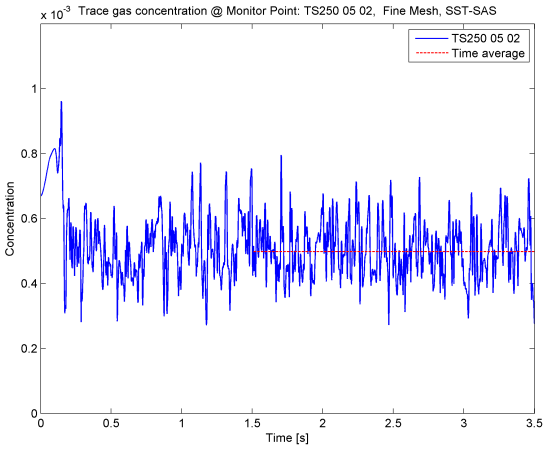

(f) *SST-SAS, fine mesh*

Figure 4.4: *Time history of trace gas concentration at monitor point 250 05 05, coarse and fine mesh (red dotted line indicates time averaging period and value)*

Between the different meshes, the simulations show a general trend of higher mixing predictions with higher mesh density, exceptions being some of the cross sections for RANS and SST-SAS between the original and fine mesh (Table 4.1). Further, the difference in solution between meshes is most evident between the coarse

and original. This could partly be explained by that the difference in meshes is larger between the coarse and original than between the original and fine, but it could also indicate that the trend is stagnating and that the different models are converging to their respective grid independent solutions.

It can be seen from Table 4.1 that the RANS and URANS simulations produce somewhat similar results also on the finer meshes. However, it seems as if the flow field is of such transient nature that the RANS model is unable to converge into a steady state solution (see the oscillating values for trace gas concentration in Figure 4.4b). This idea is strengthened by the fact that the URANS model now shows a transient flow behaviour in the solution. Further, the URANS model shows a greater increase in mixing with finer mesh density compared to the RANS model, most likely due to the transition into a transient flow field solution. Nevertheless, mixing is still grossly underpredicted both by the RANS and URANS models, even on the finest mesh.

Figure 4.5 shows contour plots of trace gas concentration at the measured cross sections throughout the duct for simulations on the fine mesh. Figure 4.5a represent a time-averaged steady state RANS solution whereas Figures 4.5b and 4.5c show instantaneous concentrations. A time-averaged solution of the SST-SAS is seen in Figure 4.5d.

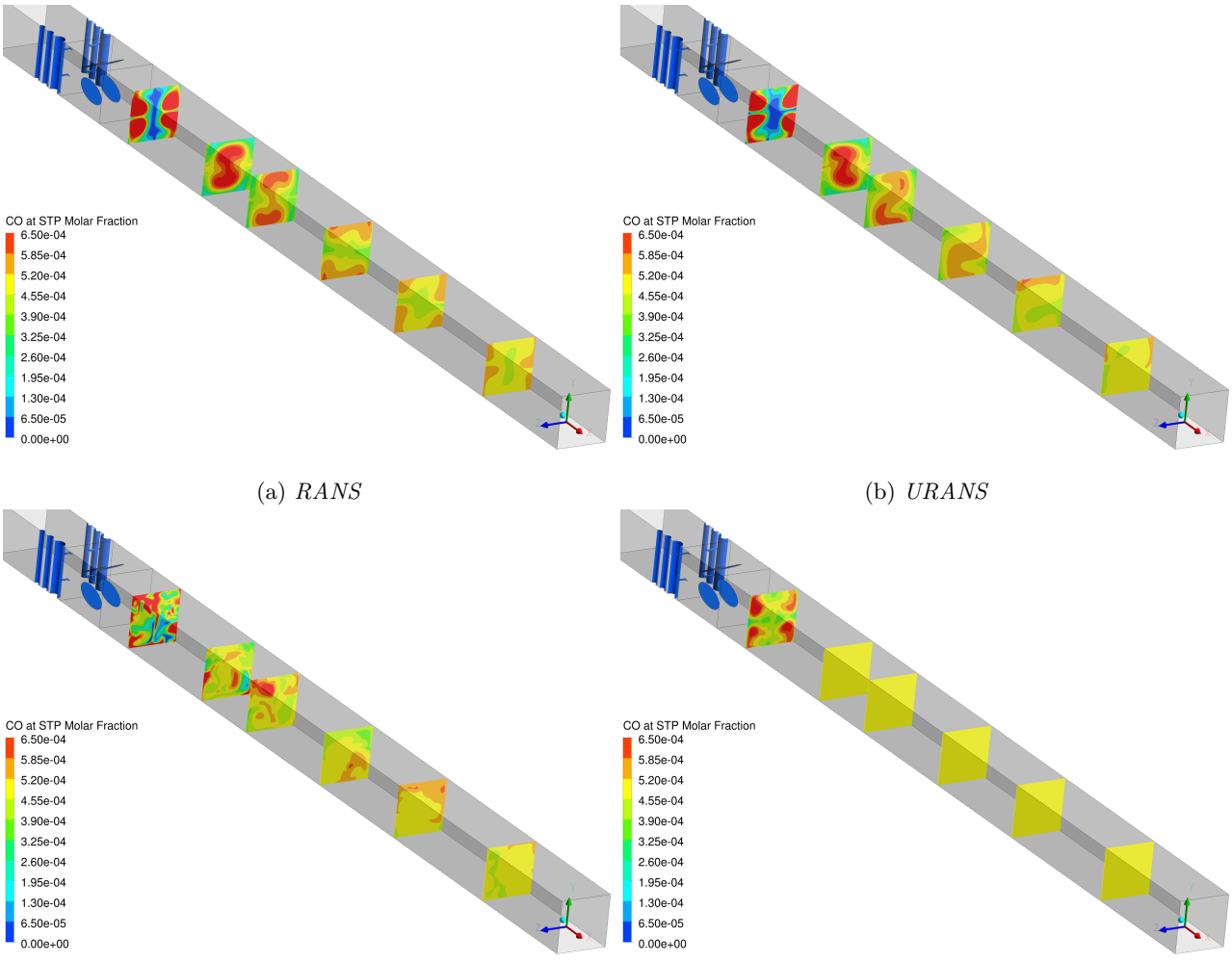

(a) *RANS*

(b) *URANS*

(c) *SST-SAS*

(d) *SST-SAS, Time averaged*

Figure 4.5: *Contour plots of trace gas concentration, fine mesh*

Again, the similarity between RANS and URANS is noticable. The concentration across the surfaces follows the same symmetrical pattern, illustrating a deficient mixing through the duct. In contrast, the SST-SAS shows chaotic and highly irregular concentration profiles over the cross sections, indicating a better mixing over the duct. This is confirmed from looking at the time-averaged SST-SAS. Here the mixing appears to be complete already at the second cross section (L/S=10), far different from the pictures of the RANS and URANS simulations.
The predicted CV of the SST-SAS is substantially lower and closer to experimental data than that of the RANS and URANS, on each of the meshes. However, with the small variation in CV on experimental data throughout the duct, it is difficult to draw any conclusions on whether the SST-SAS is accurate or if it is over predicting the mixing. To this end, a comparison between experiments and simulations on a geometry that exhibits poorer mixing (higher values on CV) or a measurement method of higher accuracy would come in use. In addition, that would help to understand the model's ability to predict mixing trends correctly.

Contour plots and history plots of trace gas concentration for simulations on the original mesh can be found in Appendix C.

4.3 Pressure loss

The pressure loss over the mixers is calculated by subtracting the pressure loss for flow without mixers in the geometry from the pressure loss over the duct with mixers present. The results from the simulations are summarized in Table 4.2 with the calculated values for pressure loss over mixer stated in the rightmost column. The results are noted to be in good agreement with experimental data for all turbulence models, with the pressure loss over mixers on the finest mesh differing less than 10 % from test values. Not surprisingly, the coarse mesh is predicting the lowest pressure losses. In the RANS formulation, pressure loss is dependent on the gradients of velocity and a coarse mesh has less ability to capture gradients, thus underpredicts the pressure loss.

It is also noted that the transient flow solutions consistently predicts lower pressure losses than the steady state (RANS) solutions. For this reason, the predicted pressure drop over the mixers for a SST-SAS simulation gets misleading, since the pressure drop over the duct without mixers is still based on a RANS simulation. However, based on the assumption that SST-SAS predicts lower pressure losses also for the empty duct flow, when predicting pressure loss over the mixers using only SST-SAS, results are likely to be even more accurate.

Table 4.2: Pressure loss

Mesh	**Simulation model**	$\Delta P_{\mathbf{System}}[Pa]$	$\Delta P_{\mathrm{Mixer}}[Pa]$
	Experiment		151
Coarse, no mixer	RANS	60.8	
Coarse	RANS	191.3	130.5
	URANS	191.3	130.5
	SST-SAS	180.3	119.4
Original, no mixer	RANS	93.3	
Original	RANS	235.4	142.1
	URANS	212.9	119.6
	SST-SAS	205.9	112.5
Fine, no mixer	RANS	70.7	
Fine	RANS	233.3	162.6
	URANS	212.5	141.8
	SST-SAS	208.8	138.2

4.4 Convergence and computational cost

As can be seen from residual plots in Figure 4.6a, the RANS simulation on the coarse mesh requires about 500 iterations to converge. The RANS simulation fails to converge, but instead oscillates around a steady state solution. Final state is reached at about 1000 iterations (see Figure 4.4b).

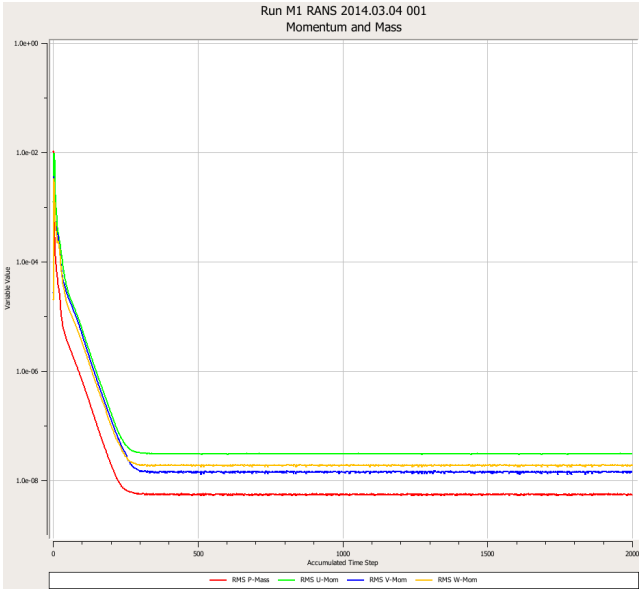

(a) *Coarse mesh*

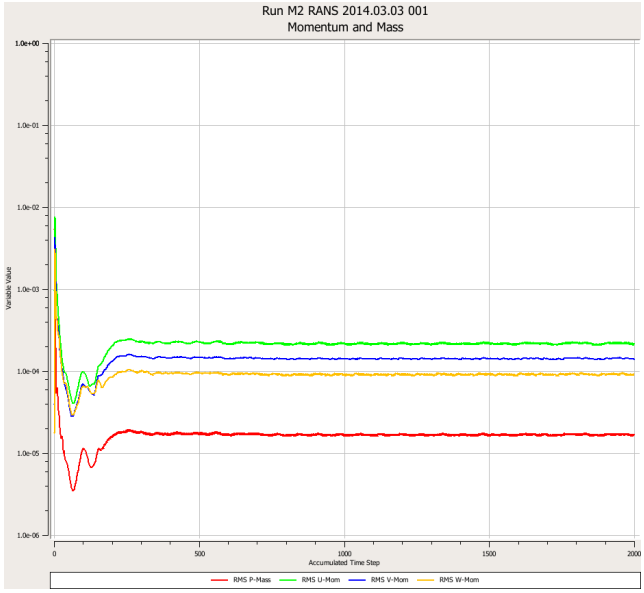

(b) *Original mesh*

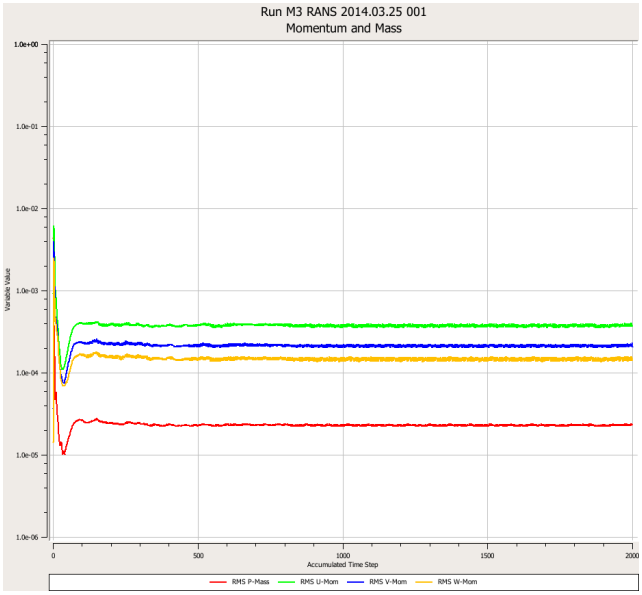

(c) *Fine Mesh*

Figure 4.6: *Mass and momentum residuals for RANS simulations*

Figure 4.7 shows the time history of trace gas concentration over the iterations between time steps for a number of monitor points for the SST-SAS simulation on the finest mesh. It demonstrate convergence on each time step as the curves are seen to flatten out. It is also seen in Table 4.3 that the URANS model produces the same results for both 2.5 ms and 1 ms time steps, indicating that 2.5 ms is a small enough time step for the URANS simulations.

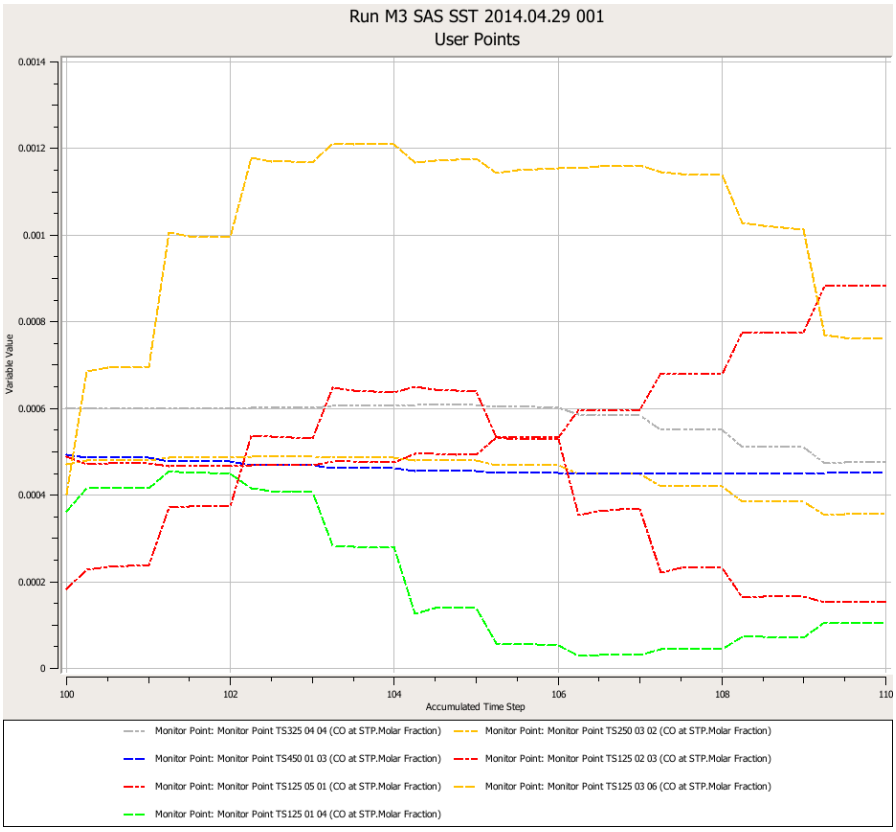

Figure 4.7: *Coefficient loop convergence for SST-SAS, fine mesh*

Table 4.3: Mixing results for URANS with different time step sizes, fine mesh

Mesh	**Simulation model**	**CV125, L/S=5**	**CV250, L/S=10**	**CV325, L/S=13**	**CV450, L/S=18**	**CV575, L/S=23**	**CV725, L/S=28**
Fine	URANS (1 ms)	66.8 %	15.0 %	9.9 %	5.0 %	3.3 %	2.4 %
Fine	URANS (2.5 ms)	65.4 %	14.5 %	9.4 %	5.1 %	3.3 %	2.1 %

When comparing computational cost between the different models, there are many factors to take into account. This includes simulation length, time step size, iterations per time step (iterations to convergence for steady/final state simulations) as well as CPU performance. In this study, some simulations were sent to and run on a high performance cluster (HPC) and some simulations were run on a desktop. The latter showed higher performance per CPU core, making a comparison between different simulations difficult. However, all the simulations on the original mesh were run on the same machine (desktop). Thus they will form the basis when evaluating the computational cost between different models.

The total CPU time for the RANS simulations was 27 h, 130 h and 409 h for the coarse, original and fine mesh respectively. As the final state was reached at about 500 iterations for the coarse mesh RANS simulation and 1000 iterations for the original and fine mesh this translates to a computational time of approximately 6 h, 66 h and 204 h. However, as the simulation on the fine mesh was run on a different machine (the HPC), it can therefore not be compared on equal terms.

As for the CPU time for URANS and SST-SAS, it is noted that the SST-SAS is about 2.75 times as costly on the original mesh. This increased computational cost is likely to be due to the difference in time step size, and not the model itself. Indeed, when time steps for URANS were decreased from 2.5 ms to 1 ms, the total CPU time increased by a factor 2.5 (see Table 4.5). However, one can argue that in order to benefit from the advantages of the SST-SAS it is required to use smaller time steps. Further, comparing the SST-SAS with the RANS model on the original mesh, the SST-SAS is seen to be 15 times more costly, assuming that the RANS simulation converges after 1000 iterations. On the other hand, when comparing SST-SAS on the coarse mesh with RANS on the fine grid (1000 iterations), SST-SAS is roughly 2.5 times more expensive, but provides far better results. Furthermore, if the SST-SAS model was to be tuned better in terms of time step settings and simulation length, computational costs could possibly be cut by a fair amount.

Table 4.4 provides a summary of total CPU time for the different simulations and information on the Courant number for the transient simulations.

Table 4.4: Computational time for the different simulations

Mesh	**Simulation model**	**Iterations/ Simulation time**	**CPU time** $[h]$	**RMS Courant no.**	**Max Courant no.**	**CPU**
Coarse, no mixer	RANS	2000	31			HPC
Original, no mixer	RANS	2000	100			Desktop
Fine, no mixer	RANS	2000	381			HPC
Coarse	RANS	2000	27			Desktop
	URANS	3.5 s	81	6.1	153.8	Desktop
	SST-SAS	3.5 s	511	2.5	62.8	HPC
Original	RANS	2000	130			Desktop
	URANS	3.5 s	355	20.9	426.8	Desktop
	SST-SAS	3.5 s	974	8.3	173.0	Desktop
Fine	RANS	2000	409			HPC
	URANS	3.5 s	466	20.9	430.6	Desktop
	SST-SAS	3.5 s	3328	8.3	173.0	HPC
	0.4 %	0.2 %				

Table 4.5: Computational time for URANS simulations with different time step size

Mesh	**Simulation model**	**Iterations/ Simulation time**	**CPU time** $[h]$	**RMS Courant no.**	**Max Courant no.**	**CPU**
Fine	URANS (2.5 ms)	3.5 s	466	20.9	430.6	Desktop
Fine	URANS (1 ms)	3.5 s	1181	8.4	176.9	Desktop

5 Conclusions

This thesis has evaluated how the turbulence models $k-\omega$ SST (steady and unsteady) and $k-\omega$ SST-SAS are capable of predicting mixing and pressure loss with different mesh densities on a computational model of a SCR test rig. It was shown that it is possible to achieve good mixing in CFD and that if the model is set up properly, one can obtain reasonably good accuracy both in terms of mixing and pressure drop.

Results show that all models are sufficiently accurate in predicting pressure loss, differing less than 10 % from experimental data on the finest mesh.

Both steady state and unsteady $k-\omega$ SST fail to reproduce the turbulent behaviour of the flow and underpredict the mixing significantly. The $k-\omega$ SST-SAS was the only model to show satisfactory agreement with experimental data in terms of mixing. It was shown to be considerably more accurate on the coarse mesh than steady state $k-\omega$ SST on the fine mesh, costing about 2.5 times as much in computational time. Further, if some time and effort is spent on tuning time step and simulation time settings, the total CPU time can likely be reduced considerably. Thus, although more computationally demanding than RANS models, it was concluded to be more efficient to use turbulence models designed for resolving turbulent motion on a coarse mesh than using time averaging turbulence models on finer meshes.

A topic of future studies is to investigate further whether the $k-\omega$ SST-SAS is able to predict mixing trends for different geometries. This is a crucial feature for the turbulence model to possess in order to be useful in the process of developing mixers. Such a study is suggested to be performed on a less efficient mixer with higher values of CV throughout the duct, or on measurements with higher accuracy at low concentrations, as this would simplify distinguishing trends in CV and ultimately the accuracy of the computational model.

References

[1] J. Mathieu and J. Scott. *An introduction to turbulent flow*. Cambridge University Press, 2000.

[2] H. K. Versteeg and W. Malalasekera. *An introduction to Computational Fluid Dynamics: The Finite Volume Method*. Pearson Education, 2007.

[3] F. R. Menter. Two-equation eddy-viscosity turbulence models for engineering applications. *AIAA journal* **32**.8 (1994), 1598–1605.

[4] J. C. Kok. Resolving the dependence on freestream values for the k-turbulence model. *AIAA journal* **38**.7 (2000), 1292–1295.

[5] L. Davidson. *Fluid mechanics, turbulent flow and turbulence modeling*. 2014. URL: http://www.tfd.chalmers.se/~lada/postscript_files/solids-and-fluids_turbulent-flow_turbulence-modelling.pdf (visited on 03/26/2014).

[6] F. R. Menter and Y. Egorov. "A Scale-Adaptive Simulation Model using Two-Equation Models". 43rd AIAA Aerospace Science Meeting and Exhibit. Reno, NV, Jan. 2005.

[7] F. Menter and Y. Egorov. The Scale-Adaptive Simulation Method for Unsteady Turbulent Flow Predictions. Part 1: Theory and Model Description. English. *Flow, Turbulence and Combustion* **85**.1 (2010), 113–138. ISSN: 1386-6184. DOI: 10.1007/s10494-010-9264-5. URL: http://dx.doi.org/10.1007/s10494-010-9264-5.

[8] Y. Egorov et al. The Scale-Adaptive Simulation Method for Unsteady Turbulent Flow Predictions. Part 2: Application to Complex Flows. English. *Flow, Turbulence and Combustion* **85**.1 (2010), 139–165. ISSN: 1386-6184. DOI: 10.1007/s10494-010-9265-4. URL: http://dx.doi.org/10.1007/s10494-010-9265-4.

[9] F. Chuiton et al. "Computation of the Helicopter Fuselage Wake with the SST, SAS, DES and XLES Models". *Advances in Hybrid RANS-LES Modelling*. Ed. by S.-H. Peng and W. Haase. Vol. 97. Notes on Numerical Fluid Mechanics and Multidisciplinary Design. Springer Berlin Heidelberg, 2008, pp. 117–124. ISBN: 978-3-540-77813-4. DOI: 10.1007/978-3-540-77815-8_12. URL: http://dx.doi.org/10.1007/978-3-540-77815-8_12.

[10] A. Widenhorn et al. "Numerical Investigation of a Laboratory Combustor Applying Hybrid RANS-LES Methods". *Advances in Hybrid RANS-LES Modelling*. Ed. by S.-H. Peng and W. Haase. Vol. 97. Notes on Numerical Fluid Mechanics and Multidisciplinary Design. Springer Berlin Heidelberg, 2008, pp. 152–161. ISBN: 978-3-540-77813-4. DOI: 10.1007/978-3-540-77815-8_16. URL: http://dx.doi.org/10.1007/978-3-540-77815-8_16.

[11] S. Šarić et al. "Comparative Assessment of Hybrid LES/RANS Models in Turbulent Flows Separating from Smooth Surfaces". *Advances in Hybrid RANS-LES Modelling*. Ed. by S.-H. Peng and W. Haase. Vol. 97. Notes on Numerical Fluid Mechanics and Multidisciplinary Design. Springer Berlin Heidelberg, 2008, pp. 142–151. ISBN: 978-3-540-77813-4. DOI: 10.1007/978-3-540-77815-8_15. URL: http://dx.doi.org/10.1007/978-3-540-77815-8_15.

[12] Y. Egorov and F. Menter. "Development and Application of SST-SAS Turbulence Model in the DESIDER Project". *Advances in Hybrid RANS-LES Modelling*. Ed. by S.-H. Peng and W. Haase. Vol. 97. Notes on Numerical Fluid Mechanics and Multidisciplinary Design. Springer Berlin Heidelberg, 2008, pp. 261–270. ISBN: 978-3-540-77813-4. DOI: 10.1007/978-3-540-77815-8_27. URL: http://dx.doi.org/10.1007/978-3-540-77815-8_27.

[13] L. Davidson. "Evaluation of the SST-SAS model: channel flow, asymmetric diffuser and axi-symmetric hill". *ECCOMAS CFD*. 2006, pp. 5–8.

[14] L. Davidson. The SAS model: A turbulence model with controlled modelled dissipation. *20th Nordic Seminar on Computational Mechanics, 20-23 Nov 2007, Göteborg* (2007).

[15] T. Blacker. "Meeting the challenge for automated conformal hexahedral meshing". *9th international meshing roundtable*. Citeseer. 2000, pp. 11–20.

[16] *ANSYS CFX-Solver Theory Guide*. Version release 14.5. Ansys, CFX. ANSYS Inc., 2012.

A Original Mesh

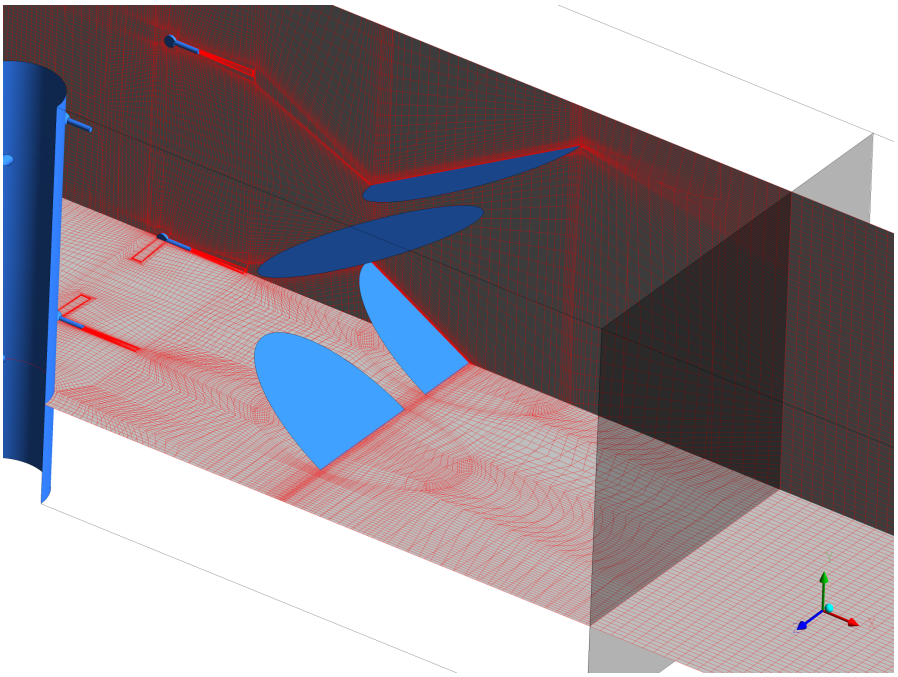

Figure A.1: *Side view of original mesh at two planes through the center of a mixer plate. Shadowed sections indicate grid interfaces*

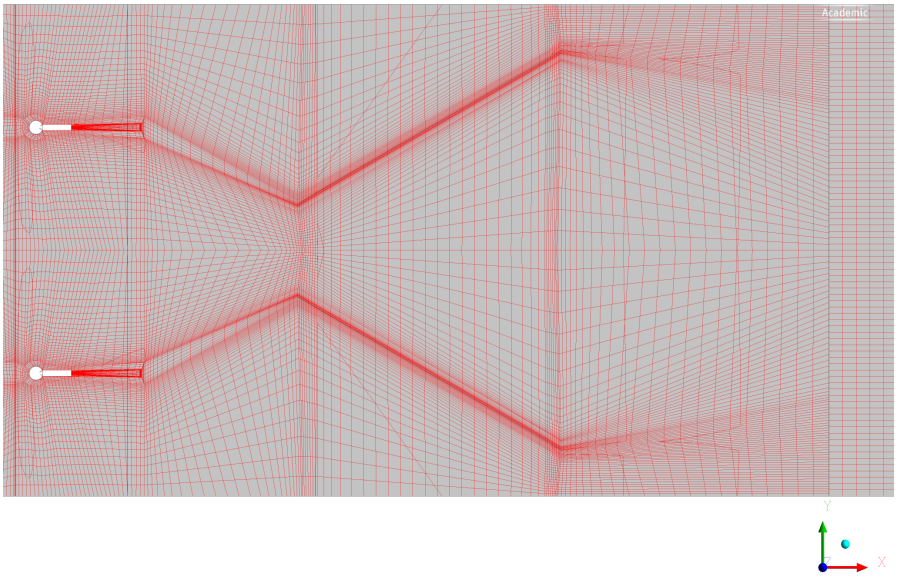

Figure A.2: *View of original mesh at X-Y plane through the center of a mixer plate*

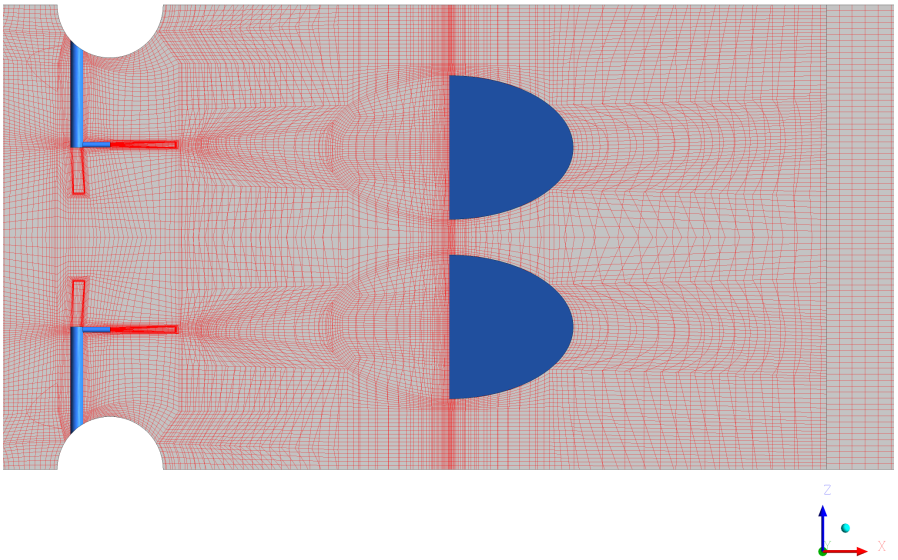

Figure A.3: *View of original mesh at X-Z plane through the center of a mixer plate*

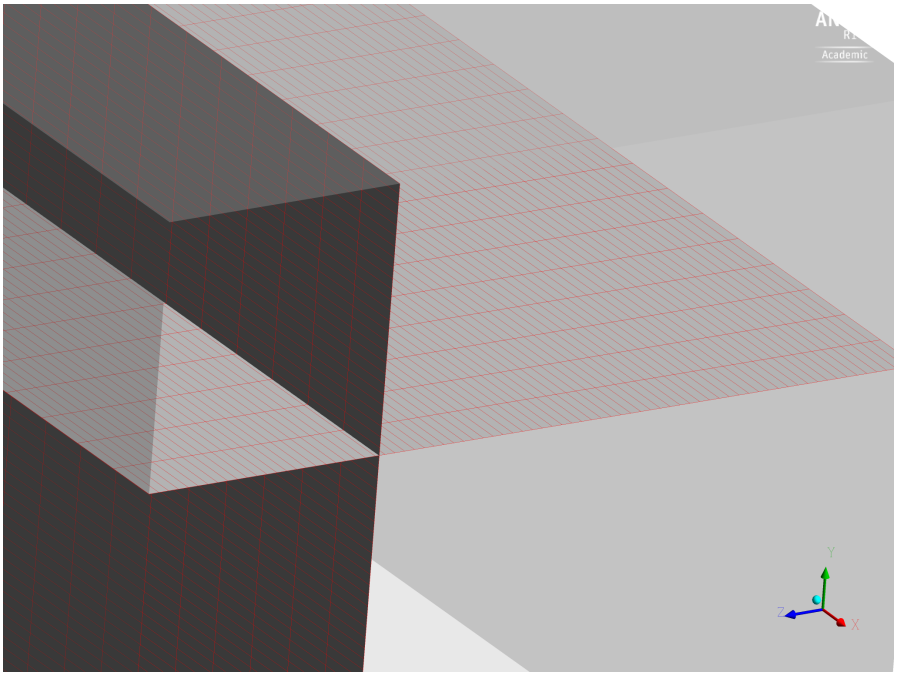

Figure A.4: *Plane sections illustrating mesh aspect ratio at duct outlet on original mesh*

B Flow field - Original mesh

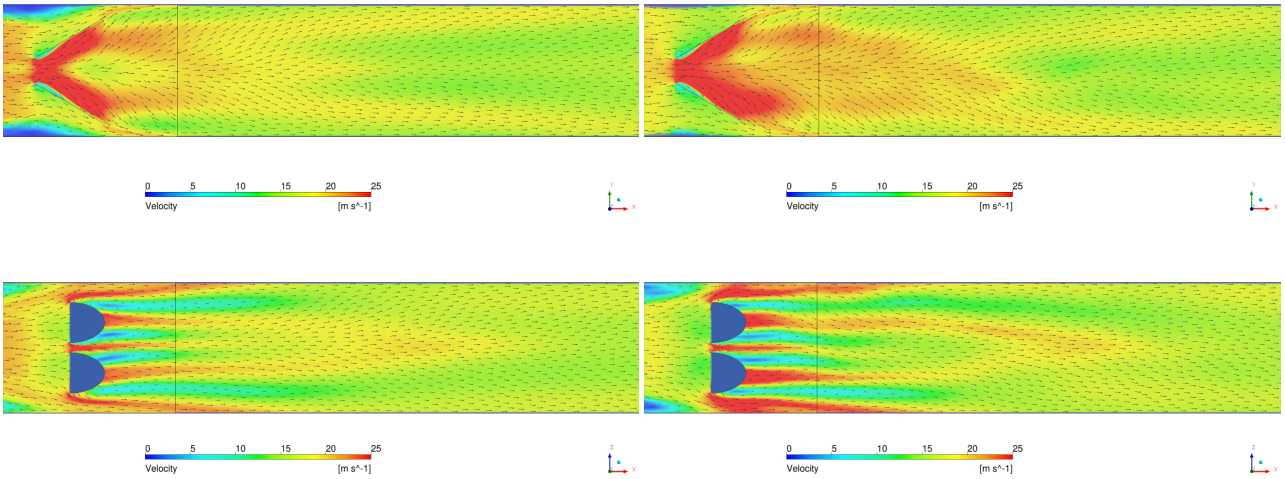

(a) *RANS* (b) *URANS*

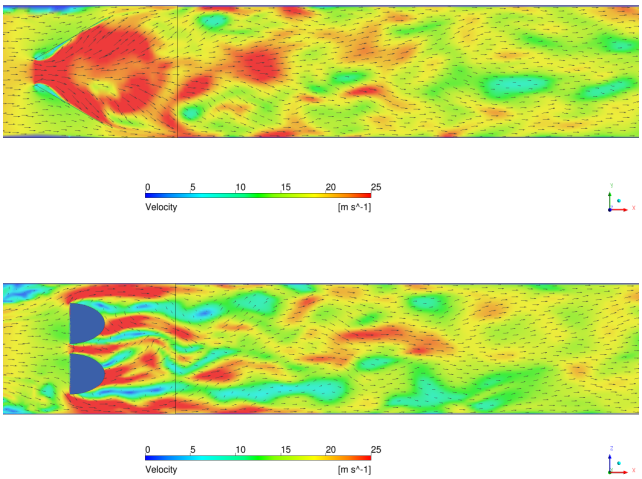

(c) *SST-SAS*

Figure B.1: *Velocity magnitude at X-Y and X-Z cross sections, original mesh*

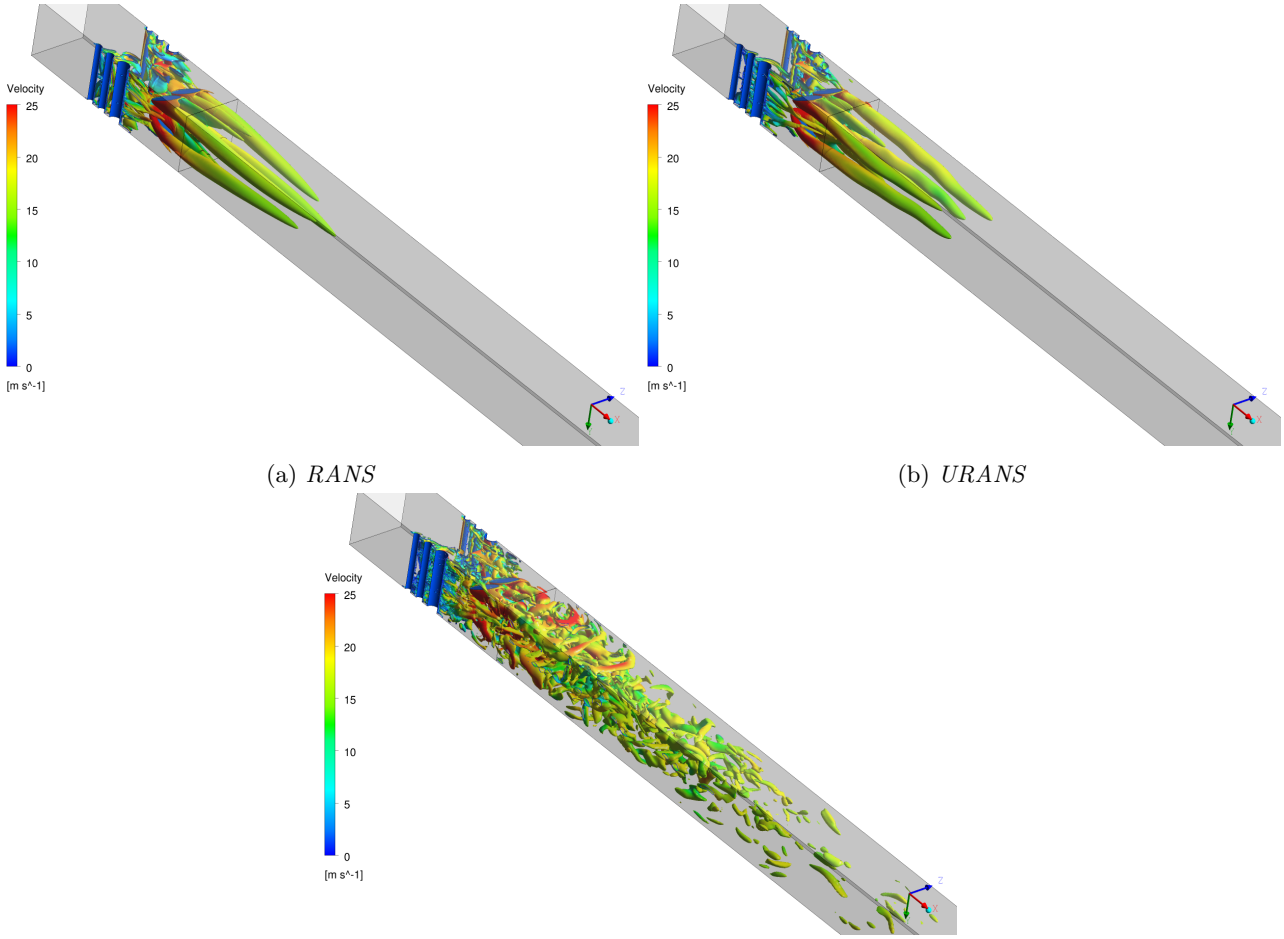

(a) *RANS* (b) *URANS*

(c) *SST-SAS*

Figure B.2: *Iso surfaces of Q=5000, original mesh (color indicates velocity magnitude)*

C Mixing - Original mesh

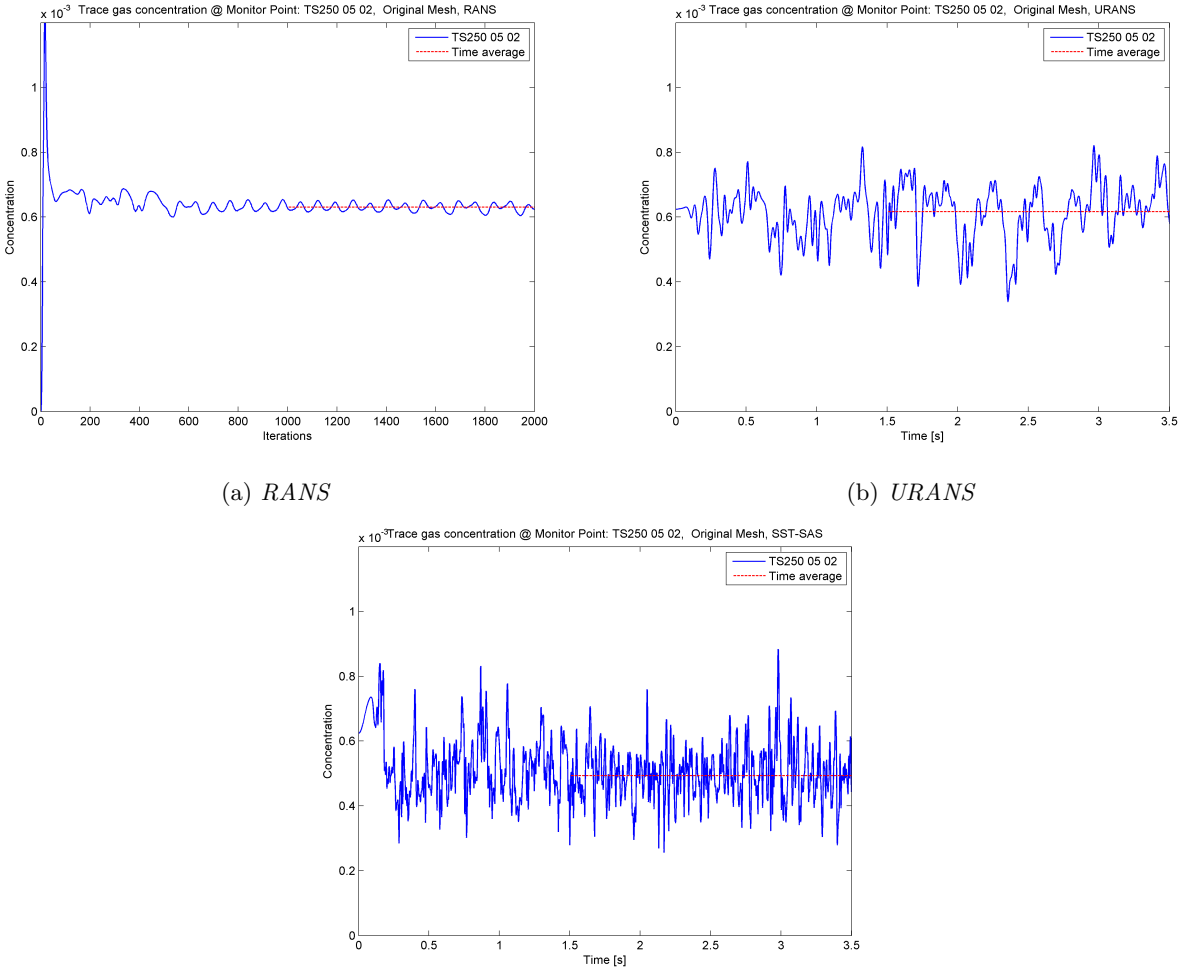

(a) *RANS*

(b) *URANS*

(c) *SST-SAS*

Figure C.1: *Time history of trace gas concentration at monitor point 250 05 05, original mesh (red dotted line indicates time averaging period and value)*

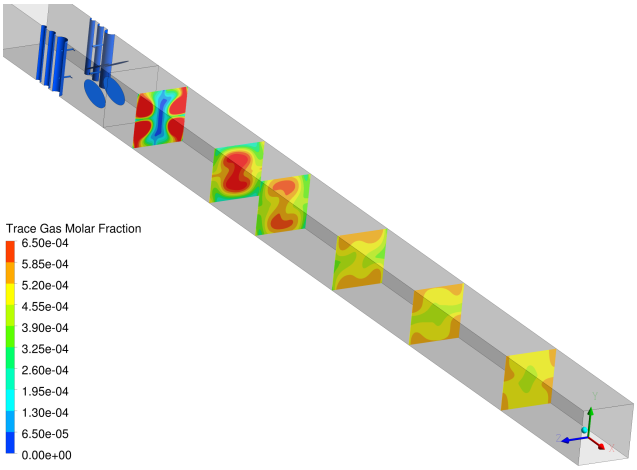

(a) *RANS*

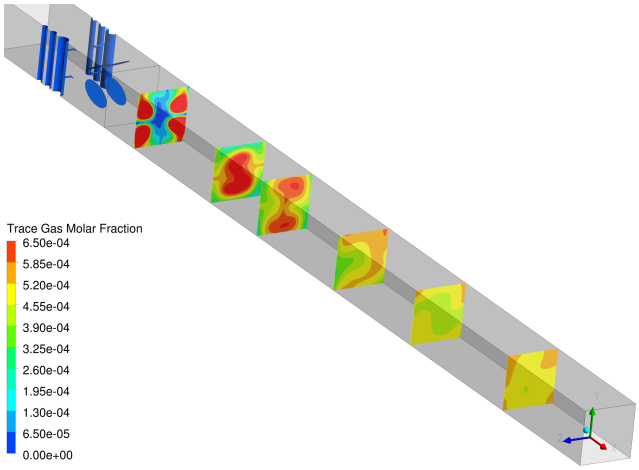

(b) *URANS*

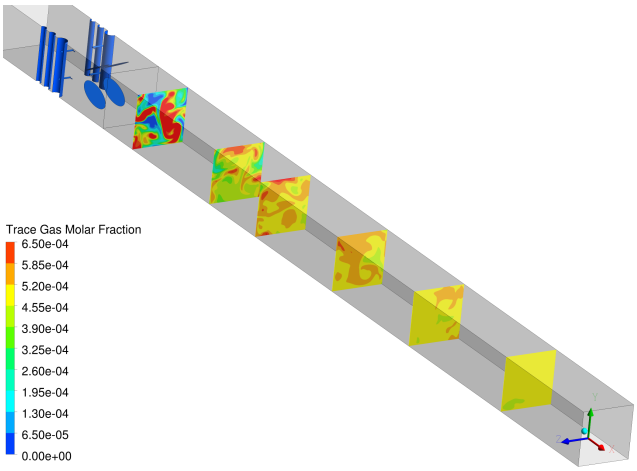

(c) *SST-SAS*

Figure C.2: *Contour plots of trace gas concentration, original mesh*